The Astrophysical Journal, 694:1643–1663, 2009 April 1 doi:10.1088/0004-637X/694/2/1643

MASS AND HOT BARYONS IN MASSIVE GALAXY CLUSTERS FROM SUBARU WEAK-LENSING AND AMiBA SUNYAEV–ZEL'DOVICH EFFECT OBSERVATIONS*

Keiichi Umetsu[1,2], Mark Birkinshaw[3], Guo-Chin Liu[1,4], Jiun-Huei Proty Wu[2,5], Elinor Medezinski[6], Tom Broadhurst[6], Doron Lemze[6], Adi Zitrin[6], Paul T. P. Ho[1,7], Chih-Wei Locutus Huang[2,5], Patrick M. Koch[1], Yu-Wei Liao[2,5], Kai-Yang Lin[1,5], Sandor M. Molnar[1], Hiroaki Nishioka[1], Fu-Cheng Wang[2,5], Pablo Altamirano[1], Chia-Hao Chang[1], Shu-Hao Chang[1], Su-Wei Chang[1], Ming-Tang Chen[1], Chih-Chiang Han[1], Yau-De Huang[1], Yuh-Jing Hwang[1], Homin Jiang[1], Michael Kesteven[8], Derek Y. Kubo[1], Chao-Te Li[1], Pierre Martin-Cocher[1], Peter Oshiro[1], Philippe Raffin[1], Tashun Wei[1], and Warwick Wilson[8]

[1] Institute of Astronomy and Astrophysics, Academia Sinica, P.O. Box 23-141, Taipei 10617, Taiwan
[2] Leung Center for Cosmology and Particle Astrophysics, National Taiwan University, Taipei 10617, Taiwan
[3] Department of Physics, University of Bristol, Tyndall Avenue, Bristol BS8 1TL, UK
[4] Department of Physics, Tamkang University, 251-37 Tamsui, Taipei County, Taiwan
[5] Department of Physics, National Taiwan University, Taipei 10617, Taiwan
[6] School of Physics and Astronomy, Tel Aviv University, Tel Aviv 69978, Israel
[7] Harvard-Smithsonian Center for Astrophysics, 60 Garden Street, Cambridge, MA 02138, USA
[8] Australia Telescope National Facility, P.O. Box 76, Epping NSW 1710, Australia
Received 2008 October 8; accepted 2009 January 5; published 2009 March 25

ABSTRACT

We present a multiwavelength analysis of a sample of four hot ($T_X > 8$ keV) X-ray galaxy clusters (A1689, A2261, A2142, and A2390) using joint AMiBA Sunyaev–Zel'dovich effect (SZE) and Subaru weak-lensing observations, combined with published X-ray temperatures, to examine the distribution of mass and the intracluster medium (ICM) in massive cluster environments. Our observations show that A2261 is very similar to A1689 in terms of lensing properties. Many tangential arcs are visible around A2261, with an effective Einstein radius $\sim 40''$ (at $z \sim 1.5$), which when combined with our weak-lensing measurements implies a mass profile well fitted by a Navarro–Frenk–White model with a high concentration $c_{\rm vir} \sim 10$, similar to A1689 and to other massive clusters. The cluster A2142 shows complex mass substructure, and displays a shallower profile ($c_{\rm vir} \sim 5$), consistent with detailed X-ray observations which imply recent interaction. The AMiBA map of A2142 exhibits an SZE feature associated with mass substructure lying ahead of the sharp northwest edge of the X-ray core suggesting a pressure increase in the ICM. For A2390 we obtain highly elliptical mass and ICM distributions at all radii, consistent with other X-ray and strong-lensing work. Our cluster gas fraction measurements, free from the hydrostatic equilibrium assumption, are overall in good agreement with published X-ray and SZE observations, with the sample-averaged gas fraction of $\langle f_{\rm gas}(< r_{200})\rangle = 0.133 \pm 0.027$, for our sample with $\langle M_{\rm vir}\rangle = (1.2 \pm 0.1) \times 10^{15}\, M_\odot\, h^{-1}$. When compared to the cosmic baryon fraction $f_b = \Omega_b/\Omega_m$ constrained by the *WMAP* five-year data, this indicates $\langle f_{\rm gas,200}\rangle / f_b = 0.78 \pm 0.16$, i.e., $(22 \pm 16)\%$ of the baryons are missing from the hot phase of clusters.

Key words: cosmic microwave background – cosmology: observations – galaxies: clusters: individual (A1689, A2142, A2261, A2390) – gravitational lensing

1. INTRODUCTION

Clusters of galaxies, the largest virialized systems known, are key tracers of the matter distribution in the large-scale structure of the universe. In the standard picture of cosmic structure formation, clusters are mostly composed of dark matter (DM) as indicated by a great deal of observational evidence, with the added assumptions that DM is nonrelativistic (cold) and collisionless, referred to as CDM. The bulk of the baryons in clusters resides in the X-ray emitting intracluster medium (ICM), where the X-ray surface brightness traces the gravitational mass dominated by DM. The remaining baryons are in the form of luminous galaxies and faint intracluster light (Fukugita et al. 1998; Gonzalez et al. 2005). Since rich clusters represent high-density peaks in the primordial fluctuation field, their baryonic mass fraction and its redshift dependence can in principle be used to constrain the background cosmology (e.g., Sasaki 1996; Allen et al. 2002, 2004, 2008). In particular, the gas mass to total mass ratio (the gas fraction) in clusters can be used to place a lower limit on the cluster baryon fraction, which is expected to match the cosmic baryon fraction, $f_b \equiv \Omega_b/\Omega_m$. However, nongravitational processes associated with cluster formation, such as radiative gas cooling and active galactic nucleus (AGN) feedback, would break the self-similarities in cluster properties, which can cause the gas fraction to acquire some mass dependence (Bialek et al. 2001; Kravtsov et al. 2005).

The deep gravitational potential wells of massive clusters generate weak shape distortions of the images of background sources due to differential deflection of light rays, resulting in a systematic distortion pattern around the centers of massive clusters, known as weak gravitational lensing (e.g., Umetsu et al. 1999; Bartelmann & Schneider 2001). In the past decade, weak lensing has become a powerful, reliable measure to map the distribution of matter in clusters, dominated by invisible DM, without requiring any assumption about the physical/dynamical state of the system (e.g., Clowe et al. 2006; Okabe & Umetsu 2008). Recently, cluster weak lensing has been used to examine the form of DM density profiles (e.g., Broadhurst et al. 2005a, 2008; Mandelbaum et al. 2008; Umetsu & Broadhurst 2008),

* Based in part on data collected at the Subaru Telescope, which is operated by the National Astronomical Society of Japan.

aiming for an observational test of the equilibrium density profile of DM halos and the scaling relation between halo mass and concentration, predicted by *N*-body simulations in the standard Λ cold dark matter (ΛCDM) model (Spergel et al. 2007; Komatsu et al. 2009). Observational results show that the form of lensing profiles in relaxed clusters is consistent with a continuously steepening density profile with increasing radius, well described by the general Navarro–Frenk–White (NFW) model (Navarro et al. 1997), expected for collisionless CDM halos.

The Yuan-Tseh Lee Array for Microwave Background Anisotropy (Ho et al. 2009) is a platform-mounted interferometer array of up to 19 elements operating at 3 mm wavelength, specifically designed to study the structure of the cosmic microwave background (CMB) radiation. In the course of early AMiBA operations, we conducted Sunyaev–Zel'dovich effect (SZE) observations at 94 GHz toward six massive Abell clusters with the seven-element compact array (Wu et al. 2009). At 94 GHz, the SZE signal is a temperature decrement in the CMB sky, and is a measure of the thermal gas pressure in the ICM integrated along the line of sight (Birkinshaw 1999; Rephaeli 1995). Therefore it is rather insensitive to the cluster core as compared with the X-ray data, allowing us to trace the distribution of the ICM out to large radii.

This paper presents a multiwavelength analysis of four nearby massive clusters in the AMiBA sample, A1689, A2261, A2142, and A2390, for which high-quality deep Subaru images are available for accurate weak-lensing measurements. This AMiBA-lensing sample represents a subset of the high-mass clusters that can be selected by their high ($T_X > 8$ keV) gas temperatures (Wu et al. 2009). Our joint weak-lensing and SZE observations, combined with supporting X-ray information available in the published literature, will allow us to constrain the cluster gas fractions without the assumption of hydrostatic equilibrium (Myers et al. 1997; Umetsu et al. 2005), complementing X-ray based studies. Our companion papers complement details of the instruments, system performance and verification, observations and data analysis, and early scientific results from AMiBA. Ho et al. (2009) describe the design concepts and specifications of the AMiBA telescope. Technical aspects of the instruments are described in Chen et al. (2009) and Koch et al. (2009a). Details of the first SZE observations and data analysis are presented in Wu et al. (2009). Nishioka et al. (2009) assess the integrity of AMiBA data with several statistical tests. Lin et al. (2009) discuss the system performance and verification. Liu et al. (2009) examine the levels of contamination from foreground sources and the primary CMB radiation. Koch et al. (2009b) present a measurement of the Hubble constant, H_0, from AMiBA SZE and X-ray data. Huang et al. (2009) discuss cluster scaling relations between AMiBA SZE and X-ray observations.

The paper is organized as follows. In Section 2, we briefly summarize the basis of cluster SZE and weak lensing. In Section 3, we present a concise summary of the AMiBA target clusters and observations. In Section 4, we describe our weak-lensing analysis of Subaru imaging data, and derive lensing distortion and mass profiles for individual clusters. In Section 5, we examine and compare cluster ellipticity and orientation profiles on mass and ICM structure in the Subaru weak-lensing and AMiBA SZE observations. In Section 6, we present our cluster models and method for measuring cluster gas fraction profiles from joint weak-lensing and SZE observations, combined with published X-ray temperature measurements; we then derive cluster gas fraction profiles, and constrain the sample-averaged gas fraction profile for our massive AMIBA-lensing clusters. Finally, a discussion and summary is given in Section 7.

Throughout this paper, we adopt a concordance ΛCDM cosmology with $\Omega_m = 0.3$, $\Omega_\Lambda = 0.7$, and $h \equiv H_0/(100\,\mathrm{km\,s^{-1}\,Mpc^{-1}}) = 0.7$. Cluster properties are determined at the virial radius $r_{\rm vir}$ and radii $(r_{200}, r_{500}, r_{2500})$, corresponding to overdensities (200, 500, 2500) relative to the critical density of the universe at the cluster redshift.

2. BASIS OF CLUSTER SUNYAEV–ZEL'DOVICH EFFECT AND WEAK LENSING

2.1. Sunyaev–Zel'dovich Effect

We begin with a brief summary of the basic equations of the thermal SZE. Our notation here closely follows the standard notation of Rephaeli (1995).

The SZE is a spectral distortion of the CMB radiation resulting from the inverse Compton scattering of cool CMB photons by the hot ICM. The nonrelativistic form of the spectral change was obtained by Sunyaev–Zel'dovich (1972) from the Kompaneets equation in the nonrelativistic limit. The change in the CMB intensity $I_{\rm CMB}$ due to the SZE is written in terms of its spectral function g and of the integral of the electron pressure along the line of sight as (Rephaeli 1995; Birkinshaw 1999; Carlstrom et al. 2002)

$$\Delta I_{\rm SZE}(\nu) = I_{\rm norm}\, g[x(\nu)]\, y(\boldsymbol{\theta}), \tag{1}$$

where $x(\nu)$ is the dimensionless frequency, $x \equiv h\nu/(k_{\rm B}T_{\rm CMB}) \approx 1.66(\nu/94\,\mathrm{GHz})$, with $k_{\rm B}$ being the Boltzmann constant and $T_{\rm CMB} = 2.725$ K being the CMB temperature at the present-day epoch, $I_{\rm norm} = (2h/c^3)\,(k_{\rm B}T_{\rm CMB}/h)^2 \simeq 2.7 \times 10^8$ Jy sr^{-1}, and $y(\boldsymbol{\theta})$ is the Comptonization parameter defined as

$$y = \int_{-r_{\rm max}}^{+r_{\rm max}} dl\, \sigma_{\rm th} n_e \left(\frac{k_B T_e}{m_e c^2}\right) = \frac{\sigma_{\rm th}}{m_e c^2} \int_{-r_{\rm max}}^{+r_{\rm max}} dl\, \frac{\rho_{\rm gas}}{\mu_e m_p} k_B T_{\rm gas}, \tag{2}$$

where $\sigma_{\rm th}$, m_e, c, and μ_e are the Thomson cross section, the electron mass, the speed of light, and the mass per electron in units of proton mass m_p, respectively; for a fully ionized H–He plasma, $\mu_e = 2/(1+X) \simeq 1.14$, with X being the hydrogen primordial abundance by mass fraction, $X \simeq 0.76$; $r_{\rm max}$ is the cutoff radius for an isolated cluster (see Section 6.3). The SZE spectral function $g(x)$ is expressed as

$$g(x) = g_{\rm NR}(x)[1 + \delta_{\rm SZE}(x, T_{\rm gas})], \tag{3}$$

where $g_{\rm NR}(x)$ is the thermal spectral function in the nonrelativistic limit (Sunyaev & Zel'dovich 1972),

$$g_{\rm NR}(x) = \frac{x^4 e^x}{(e^x-1)^2}\left(x\frac{e^x+1}{e^x-1} - 4\right), \tag{4}$$

which is zero at the crossover frequency $x_0 \simeq 3.83$, or $\nu_0 = 217$ GHz, and $\delta_{\rm SZE}(x, T_{\rm gas})$ is the relativistic correction (Challinor & Lasenby 1998; Itoh et al. 1998). The fractional intensity decrease due to the SZE with respect to the primary CMB is maximized at $\nu \sim 100$ GHz (see Figure 1 of Zhang et al. 2002), which is well matched to the observing frequency range 86–102 GHz of AMiBA. At the central frequency $\nu_c = 94$ GHz of AMiBA, $g(x) \simeq -3.4$. For our hot X-ray clusters with $T_X = 8$–10 keV, the relativistic correction to the thermal SZE is 6%–7% at $\nu_c = 94$ GHz.

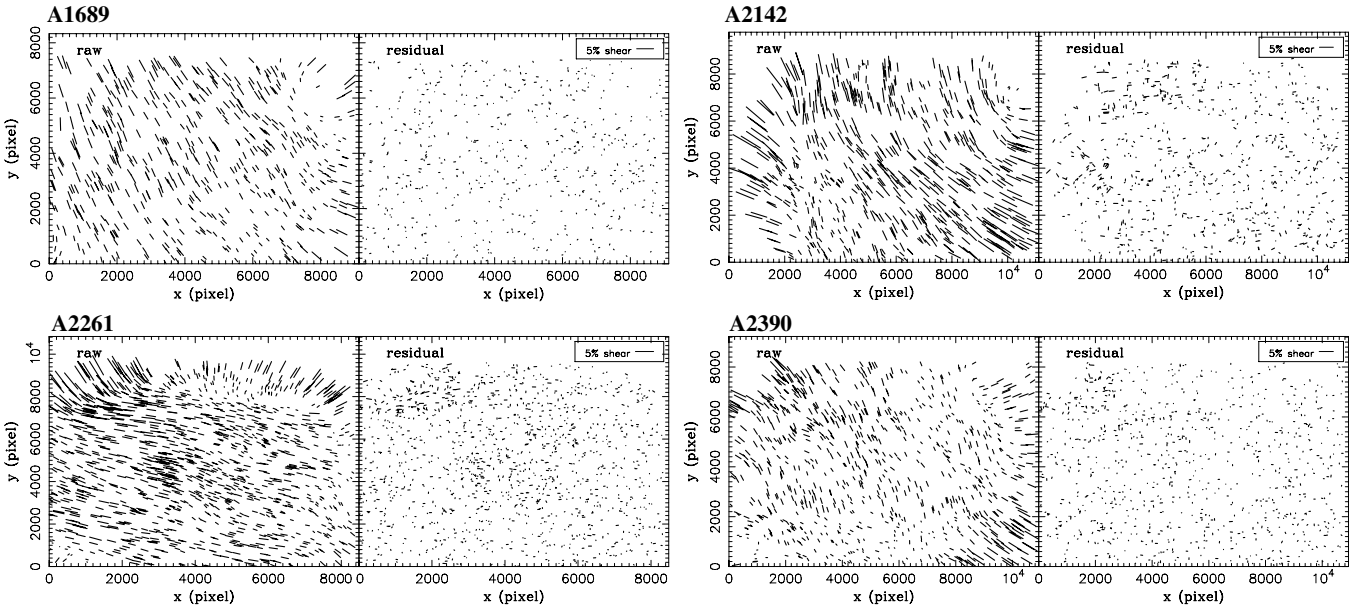

Figure 1. Quadrupole PSF anisotropy field for individual clusters as measured from stellar ellipticities before and after the PSF anisotropy correction. For each cluster field, the left panel shows the raw ellipticity field of stellar objects, and the right panel shows the residual ellipticity field after the PSF anisotropy correction. The orientation of the sticks indicates the position angle of the major axis of stellar ellipticity, whereas the length is proportional to the modulus of stellar ellipticity. A stick with the length of 5% ellipticity is indicated in the top right of the right panel.

2.2. Cluster Weak Lensing

Weak gravitational lensing is responsible for the weak shape distortion and magnification of the images of background sources due to the gravitational field of intervening foreground clusters of galaxies and large-scale structures in the universe. The deformation of the image can be described by the 2×2 Jacobian matrix $\mathcal{A}_{\alpha\beta}$ ($\alpha, \beta = 1, 2$) of the lens mapping. The Jacobian $\mathcal{A}_{\alpha\beta}$ is real and symmetric, so that it can be decomposed as

$$\mathcal{A}_{\alpha\beta} = (1 - \kappa)\delta_{\alpha\beta} - \Gamma_{\alpha\beta}, \tag{5}$$

$$\Gamma_{\alpha\beta} = \begin{pmatrix} +\gamma_1 & \gamma_2 \\ \gamma_2 & -\gamma_1 \end{pmatrix}, \tag{6}$$

where $\delta_{\alpha\beta}$ is Kronecker's delta, $\Gamma_{\alpha\beta}$ is the trace-free, symmetric shear matrix with γ_α being the components of spin-2 complex gravitational shear $\gamma := \gamma_1 + i\gamma_2$, describing the anisotropic shape distortion, and κ is the lensing convergence responsible for the trace part of the Jacobian matrix, describing the isotropic area distortion. In the weak-lensing limit where $\kappa, |\gamma| \ll 1$, $\Gamma_{\alpha\beta}$ induces a quadrupole anisotropy of the background image, which can be observed from ellipticities of background galaxy images. The flux magnification due to gravitational lensing is given by the inverse Jacobian determinant,

$$\mu = \frac{1}{\det \mathcal{A}} = \frac{1}{(1 - \kappa)^2 - |\gamma|^2}, \tag{7}$$

where we assume subcritical lensing, i.e., $\det \mathcal{A}(\boldsymbol{\theta}) > 0$.

The lensing convergence is expressed as a line-of-sight projection of the matter density contrast $\delta_m = (\rho_m - \bar{\rho})/\bar{\rho}$ out to the source plane (s) weighted by certain combination of comoving angular diameter distances r (e.g., Jain et al. 2000),

$$\kappa = \frac{3H_0^2\Omega_m}{2c^2} \int_0^{\chi_s} d\chi\, \mathcal{G}(\chi, \chi_s) \frac{\delta_m}{a} \equiv \int d\Sigma_m\, \Sigma_{\rm crit}^{-1}, \tag{8}$$

$$\mathcal{G}(\chi, \chi_s) = \frac{r(\chi) r(\chi_s - \chi)}{r(\chi_s)}, \tag{9}$$

where a is the cosmic scale factor, χ is the comoving distance, Σ_m is the surface mass density of matter, $\Sigma_m = \int d\chi\, a(\rho_m - \bar{\rho})$, with respect to the cosmic mean density $\bar{\rho}$, and $\Sigma_{\rm crit}$ is the critical surface mass density for gravitational lensing,

$$\Sigma_{\rm crit} = \frac{c^2}{4\pi G} \frac{D_s}{D_d D_{ds}}, \tag{10}$$

with D_s, D_d, and D_{ds} being the (proper) angular diameter distances from the observer to the source, from the observer to the deflecting lens, and from the lens to the source, respectively. For a fixed background cosmology and a lens redshift z_d, $\Sigma_{\rm crit}$ is a function of background source redshift z_s. For a given mass distribution $\Sigma_m(\boldsymbol{\theta})$, the lensing signal is proportional to the angular diameter distance ratio, D_{ds}/D_s.

In the present weak-lensing study, we aim to reconstruct the dimensionless surface mass density κ from weak-lensing distortion and magnification data. To do this, we utilize the relation between the gradients of κ and γ (Kaiser 1995; Crittenden et al. 2002),

$$\triangle\kappa(\boldsymbol{\theta}) = \partial^\alpha \partial^\beta \Gamma_{\alpha\beta}(\boldsymbol{\theta}) = 2\hat{\mathcal{D}}^* \gamma(\boldsymbol{\theta}), \tag{11}$$

where $\hat{\mathcal{D}}$ is the complex differential operator $\hat{\mathcal{D}} = (\partial_1^2 - \partial_2^2)/2 + i\partial_1\partial_2$. The Green's function for the two-dimensional Poisson equation is $\triangle^{-1}(\boldsymbol{\theta}, \boldsymbol{\theta}') = \ln|\boldsymbol{\theta} - \boldsymbol{\theta}'|/(2\pi)$, so that Equation (11) can be solved to yield the following nonlocal relation between κ and γ (Kaiser & Squires 1993):

$$\kappa(\boldsymbol{\theta}) = \frac{1}{\pi} \int d^2\theta'\, D^*(\boldsymbol{\theta} - \boldsymbol{\theta}')\gamma(\boldsymbol{\theta}'), \tag{12}$$

where $D(\boldsymbol{\theta})$ is the complex kernel defined as

$$D(\boldsymbol{\theta}) = \frac{\theta_2^2 - \theta_1^2 - 2i\theta_1\theta_2}{|\theta|^4}. \tag{13}$$

Similarly, the spin-2 shear field can be expressed in terms of the lensing convergence as

$$\gamma(\boldsymbol{\theta}) = \frac{1}{\pi}\int d^2\theta'\, D(\boldsymbol{\theta}-\boldsymbol{\theta}')\kappa(\boldsymbol{\theta}'). \quad (14)$$

Note that adding a constant mass sheet to κ in Equation (14) does not change the shear field $\gamma(\boldsymbol{\theta})$ which is observable in the weak-lensing limit, leading to the so-called *mass-sheet degeneracy* (see Equation (16)) based solely on shape-distortion measurements (e.g., Bartelmann & Schneider 2001; Umetsu et al. 1999). In general, the observable quantity is not the gravitational shear γ but the *reduced* shear,

$$g = \frac{\gamma}{1-\kappa} \quad (15)$$

in the subcritical regime, where $\det \mathcal{A} > 0$ (or $1/g^*$ in the negative parity region with $\det \mathcal{A} < 0$). We see that the reduced shear g is invariant under the following global transformation:

$$\kappa(\boldsymbol{\theta}) \to \lambda\kappa(\boldsymbol{\theta}) + 1 - \lambda, \quad \gamma(\boldsymbol{\theta}) \to \lambda\gamma(\boldsymbol{\theta}), \quad (16)$$

with an arbitrary scalar constant $\lambda \neq 0$ (Schneider & Seitz 1995).

3. AMiBA SUNYAEV–ZEL'DOVICH EFFECT OBSERVATIONS

3.1. AMiBA Telescope

The AMiBA is a dual channel 86–102 GHz (3 mm wavelength) interferometer array of up to 19 elements with dual polarization capabilities sited at 3396 m on Mauna Loa, Hawaii (latitude: +19°.5, longitude: −155°.6).[9] AMiBA is equipped with 4-lag analog, broadband (16 GHz bandwidth centered at 94 GHz) correlators which output a set of four real-number correlation signals (Chen et al. 2009). These four degrees of freedom (dof) correspond to two complex visibilities in two frequency channels. The frequency of AMiBA operation was chosen to take advantage of the optimal frequency window at 3 mm, where the fractional decrement in the SZE intensity relative to the primary CMB is close to its maximum (see Section 2.1) and contamination by the Galactic synchrotron emission, dust foregrounds, and the population of cluster/background radio sources is minimized (see for detailed contamination analysis Liu et al. 2009). This makes AMiBA a unique CMB/SZE interferometer, and also complements the wavelength coverage of other existing and planned CMB instruments: interferometers such as AMI at 15 GHz (Kneissl et al. 2001), CBI at 30 GHz (Padin et al. 2001, 2002; Mason et al. 2003; Pearson et al. 2003), SZA at 30 and 90 GHz (Mroczkowski et al. 2009), and VSA[10] at 34 GHz (Watson et al. 2003); bolometer arrays such as ACT,[11] APEX-SZ[12] (Halverson et al. 2008), and SPT.[13]

In the initial operation of AMiBA, we used seven 0.6 m (0.58 m to be precise) Cassegrain antennas (Koch et al. 2006) comounted on a 6 m hexapod platform in a hexagonal close-packed configuration (see Ho et al. 2009). At each of the frequency channels centered at about 90 and 98 GHz, this compact configuration provides 21 simultaneous baselines with three baseline lengths of $d = 0.61$, 1.05, and 1.21 m, corresponding to angular multipoles $l = 2\pi\sqrt{u^2+v^2}(= 2\pi d/\lambda)$ of $l \approx 1194, 2073, 2394$ at $\nu_c = 94$ GHz. This compact seven-element array is sensitive to multipole range $800 \lesssim l \lesssim 2600$. With 0.6 m antennas, the instantaneous field of view of AMiBA is about 23′ FWHM (Wu et al. 2009), and its angular resolution ranges from 2′ to 6′ depending on the configuration and weighting scheme. In the compact configuration, the angular resolution of AMiBA is about 6′ FWHM using *natural weighting* (i.e., inverse noise variance weighting). The point source sensitivity is estimated to be ∼ 63 mJy (Lin et al. 2009) in 1 hr of on-source integration in two-patch main-trail/lead differencing observations, where the overall noise level is increased by a factor of $\sqrt{2}$ due to the differencing.

3.2. Initial Target Clusters

The AMiBA-lensing sample, A1689, A2142, A2261, and A2390, is a subset of the AMiBA cluster sample (see Wu et al. 2009), composed of four massive clusters at relatively low redshifts of $0.09 \lesssim z \lesssim 0.23$ with a median redshift of $\bar{z} \approx 0.2$. The sample size is simply limited by the availability of high-quality Subaru weak-lensing data. A1689 is a relaxed, round system, and is one of the best studied clusters for lensing work (e.g., Broadhurst et al. 2005a; Limousin et al. 2007; Umetsu & Broadhurst 2008; Broadhurst et al. 2008). A2261 is a compact cluster with a regular X-ray morphology. A2142 is a merging cluster with two sharp X-ray surface brightness discontinuities in the cluster core (Markevitch et al. 2000; Okabe & Umetsu 2008). A2390 shows an elongated morphology both in the X-ray emission and strong-lensing mass distributions (Allen et al. 2001; Frye & Broadhurst 1998). Table 1 summarizes the physical properties of the four target clusters in this multiwavelength study.

In 2007, AMiBA with the seven small antennas (henceforth AMiBA7) was in the science verification phase. For our initial observations, we therefore selected those target clusters observable from Mauna Loa during the observing period that were known to have strong SZEs at relatively low redshifts ($0.1 \lesssim z \lesssim 0.3$) from previous experiments, such as Owens Valley Radio Observatory (OVRO) observations at 30 GHz (Mason et al. 2001), BIMA/OVRO observations at 30 GHz (Grego et al. 2001a; Reese et al. 2002), VSA observations at 34 GHz (Lancaster et al. 2005), and SuZIE II observations at 145, 221, and 355 GHz (Benson et al. 2004). The targeted redshift range allows the target clusters to be resolved by the 6′ resolution of AMiBA7, allowing us to derive useful measurements of cluster SZE profiles for our multiwavelength studies. At redshifts of $z \lesssim 0.3$ (0.2), the angular resolution of AMiBA7 corresponds to $\lesssim 560\,\mathrm{kpc}\,h^{-1}$ ($\sim 400\,\mathrm{kpc}\,h^{-1}$) in radius, which is $\lesssim$ 30%–40% (∼ 20%–30%) of the virial radius 1.5–2 Mpc h^{-1} of massive clusters. The requirement of being SZE strong is to ensure reliable SZE measurements at 3 mm with AMiBA7. We note that AMiBA and SZA are the only SZE instruments measuring at 3 mm, but complimentary in their baseline coverage. With sensitivities of 20–30 mJy beam^{-1} typically achieved in two-patch differencing observations in 5–10 hr of net on-source integration (Wu et al. 2009), we would expect $\gtrsim 5\sigma$ detections of SZE fluxes $\gtrsim$ 100–150 mJy at 3 mm. Finally, our observing period (2007 April–August) limited the range of right ascension (R.A.) of targets,[14] since we restricted our observations to nights (roughly 8 p.m. to 8 a.m.), where we would expect high

[9] http://amiba.asiaa.sinica.edu.tw/
[10] http://astro.uchicago.edu/sza/
[11] http://www.hep.upenn.edu/act/act.html
[12] http://bolo.berkeley.edu/apexsz
[13] http://pole.uchicago.edu

[14] The elevation limit of AMiBA is 30°.

Table 1
Target Clusters and AMiBA/X-ray Properties

Cluster	z	1 arcmin[a]	AMiBA7[b]		X-Ray[c]		
			SZE Flux	Image FWHM	T_X	θ_c	References
		(kpc h^{-1})	(mJy)	(arcmin)	(keV)	(arcmin)	
A1689	0.183	129.6	-168 ± 28	5.7	$9.66^{+0.22}_{-0.20}$	0.44 ± 0.01	3
A2142	0.091	71.4	-316 ± 23	9.0	9.7 ± 1.0	3.14 ± 0.22	1, 4, 5
A2261	0.224	151.8	-90 ± 17	5.8	$8.82^{+0.37}_{-0.32}$	0.26 ± 0.02	3
A2390	0.228	153.3	-158 ± 24	8.0	10.1 ± 1.1	0.47 ± 0.05	2

Notes. Uncertainties are at 68% confidence.
[a] Physical scale in kpc h^{-1} units corresponding to $1'$ at the cluster redshift.
[b] SZE properties from AMiBA7 at 94 GHz: cluster peak SZE flux (mJy) and angular size ($'$) in FWHM measured from the cleaned image (Wu et al. 2009).
[c] Published X-ray properties: X-ray temperature (keV), X-ray core radius (kpc h^{-1}), and references. For A2142, T_X and θ_c are taken from Reference [1], and References [4, 5], respectively. For A2390 a 10% error is assumed for (T_X, β), for which no error estimate was presented in the original reference.
References. [1] Markevitch et al. (1998); [2] Boehringer et al. (1998); [3] Reese et al. (2002); [4] Sanderson et al. (2003); [5] Lancaster et al. (2005).

Table 2
Subaru Weak-Lensing Data and Background Galaxy Sample

Cluster	Filters	Seeing[a]	n_g[b]	B/R[c]	$\langle D_{ds}/D_s \rangle$[d]	$z_{s,D}$[e]	σ_κ[f]
		(arcsec)	(arcmin^{-2})				
A1689	Vi'	0.88	8.8	0	0.70 ± 0.02	$0.70^{+0.06}_{-0.05}$	0.029
A2142	$g'R_c$	0.55	30.4	2.1	0.88 ± 0.04	$0.95^{+0.79}_{-0.30}$	0.021
A2261	VR_c	0.65	13.8	1.5	0.72 ± 0.04	$0.98^{+0.24}_{-0.16}$	0.032
A2390	VR_c	0.70	20.7	2.1	0.72 ± 0.04	$1.00^{+0.25}_{-0.16}$	0.026

Notes.
[a] Seeing FWHM in the final co-added image in the redder band.
[b] Surface number density of blue+red galaxies.
[c] Fraction of blue to red galaxies in the blue+red background sample.
[d] Distance ratio averaged over the redshift distribution of the blue+red sample.
[e] Effective source redshift (see Equation (22)) corresponding to the mean depth $\langle D_{ds}/D_s \rangle$.
[f] The rms noise level in the reconstructed κ map.

gain stability because the ambient temperature varies slowly and little (Nishioka et al. 2009). The SZE strong clusters in our AMiBA sample are likely to have exceedingly deep potential wells, and indeed our AMiBA sample represents a class of hot X-ray clusters with observed X-ray temperatures exceeding 8 keV (see Table 1). We note that this may affect the generality of the results presented in this study. A main-trail/lead differencing scheme has been used in our targeted cluster observations where the trail/lead (blank) field is subtracted from the main (cluster) field. This differencing scheme sufficiently removes contamination from ground spillover and electronic DC offset in the correlator output (Wu et al. 2009). A full description of AMiBA observations and analysis of the initial six target clusters, including the observation strategy, analysis methodology, calibrations, and map-making, can be found in Wu et al. (2009, 2008).

4. SUBARU WEAK-LENSING DATA AND ANALYSIS

In this section, we present a technical description of our weak-lensing distortion analysis of the AMiBA-lensing sample based on Subaru data. The present work on A1689 is based on the same Subaru images as analyzed in our earlier work of Broadhurst et al. (2005a) and Umetsu & Broadhurst (2008), but our improved color selection of the red background has increased the sample size by $\sim 16\%$ (Section 4.3). This work on A2142 is based on the same Subaru images as in Okabe & Umetsu (2008), but our inclusion of blue, as well as red, galaxies has increased the sample size by a factor of 4 (see Table 6 of Okabe & Umetsu 2008), leading to a significant improvement of our lensing measurements. For A2261 and A2390 we present our new weak-lensing analysis based on Suprime-Cam imaging data retrieved from the Subaru archive, SMOKA. The reader only interested in the main result may skip directly to Section 4.4.

4.1. Subaru Data and Photometry

We analyze deep images of four high-mass clusters in the AMiBA sample taken by the wide-field camera Suprime-Cam ($34' \times 27'$; Miyazaki et al. 2002) at the prime focus of the 8.3 m Subaru telescope. The clusters were observed deeply in two optical passbands each with seeing in the co-added images ranging from $0''.55$ to $0''.88$ (see Table 2). For each cluster, we select an optimal combination of two filters that allows for an efficient separation of cluster/background galaxies based on color–magnitude correlations (see Table 2). We use either R_c or i' band for our weak-lensing measurements (described in Section 4.2) for which the instrumental response, sky background, and seeing conspire to provide the best-quality images. The standard pipeline reduction software for Suprime-Cam (Yagi et al. 2002) is used for flat-fielding, instrumental distortion correction, differential refraction, sky subtraction and stacking. Photometric catalogs are constructed from stacked and matched images using SExtractor (Bertin & Arnouts 1996), and used for our color selection of background galaxies (see Section 4.3).

4.2. Weak-Lensing Distortion Analysis

We use the IMCAT package developed by N. Kaiser[15] to perform object detection, photometry, and shape measurements, following the formalism outlined in Kaiser et al. (1995, KSB). Our analysis pipeline is implemented based on the procedures described in Erben et al. (2001) and on verification tests with STEP1 data of mock ground-based observations (Heymans et al. 2006). The same analysis pipeline has been used in Umetsu &

[15] http://www.ifa.hawaii.edu/k˜aiser/imcat

Broadhurst (2008), Okabe & Umetsu (2008), and Broadhurst et al. (2008).

4.2.1. Object Detection

Objects are first detected as local peaks in the image by using the IMCAT hierarchical peak-finding algorithm *hfindpeaks* which for each object yields object parameters such as a peak position ($\boldsymbol{x}$), an estimate of the object size (r_g), and the significance of the peak detection (ν). The local sky level and its gradient are measured around each object from the mode of pixel values on a circular annulus defined by inner and outer radii of $16 \times r_g$ and $32 \times r_g$. In order to avoid contamination in the background estimation by bright neighboring stars and/or foreground galaxies, all pixels within $3 \times r_g$ of another object are excluded from the mode calculation. Total fluxes and half-light radii (r_h) are then measured on sky-subtracted images using a circular aperture of radius $3 \times r_g$ from the object center. Any pixels within $2.5 \times r_g$ of another object are excluded from the aperture. The aperture magnitude is then calculated from the measured total flux and a zero-point magnitude. Any objects with positional differences between the peak location and the weighted-centroid greater than $|\boldsymbol{d}| = 0.4$ pixels are excluded from the catalog.

Finally, bad objects such as spikes, saturated stars, and noisy detections need to be removed from the weak-lensing analysis. We removed from our detection catalog extremely small or large objects with $r_g < 1$ pixel or $r_g > 10$ pixels, objects with low detection significance, $\nu < 7$ (see Erben et al. 2001), objects with large raw ellipticities, $|e| > 0.5$ (see Section 4.2.2), noisy detections with unphysical negative fluxes, and objects containing more than 10 bad pixels, nbad > 10.

4.2.2. Weak-Lensing Distortion Measurements

To obtain an estimate of the reduced shear, $g_\alpha = \gamma_\alpha/(1-\kappa)$ ($\alpha = 1, 2$), we measure using the *getshapes* routine in IMCAT the image ellipticity $e_\alpha = \{Q_{11} - Q_{22}, Q_{12}\}/(Q_{11} + Q_{22})$ from the weighted quadrupole moments of the surface brightness of individual galaxies defined in the above catalog,

$$Q_{\alpha\beta} = \int d^2\theta\, W(\theta)\theta_\alpha\theta_\beta I(\boldsymbol{\theta}) \quad (\alpha, \beta = 1, 2), \tag{17}$$

where $I(\boldsymbol{\theta})$ is the surface brightness distribution of an object, $W(\theta)$ is a Gaussian window function matched to the size of the object, and the object center is chosen as the coordinate origin. In Equation (17), the maximum radius of integration is chosen to be $\theta_{\rm max} = 4r_g$.

Firstly, the point-spread function (PSF) anisotropy needs to be corrected using the star images as references :

$$e'_\alpha = e_\alpha - P^{\alpha\beta}_{\rm sm} q^*_\beta, \tag{18}$$

where $P_{\rm sm}$ is the *smear polarizability* tensor (which is close to diagonal) and $q^*_\alpha = (P^*_{\rm sm})^{-1}_{\alpha\beta} e^\beta_*$ is the stellar anisotropy kernel. We select bright, unsaturated foreground stars identified in a branch of the half-light radius versus magnitude diagram to measure q^*_α. In order to obtain a smooth map of q^*_α which is used in Equation (18), we divided the co-added mosaic image (of $\sim 10\,$K pixels $\times\, 8\,$K pixels) into rectangular blocks. The block length is based on the coherent scale of PSF anisotropy patterns, and is typically 2 K pixels. In this way, the PSF anisotropy in individual blocks can be well described by fairly low-order polynomials. We then fitted the q^* in each block independently with second-order bi-polynomials, $q^\alpha_*(\boldsymbol{\theta})$, in conjunction with iterative outlier rejection on each component of the residual: $\delta e^*_\alpha = e^*_\alpha - (P^*_{\rm sm})^{\alpha\beta} q^*_\beta(\boldsymbol{\theta})$. The final stellar sample contains typically 500–1200 stars. Uncorrected ellipticity components of stellar objects have on average a mean offset (from a value of zero) of 1%–2% with a few % of rms, or variation of PSF across the data field (see, e.g., Umetsu & Broadhurst 2008; Okabe & Umetsu 2008). On the other hand, the mean residual stellar ellipticity $\overline{\delta e^*_\alpha}$ after correction is less than or about 10^{-4}, with the standard error on this measurement a few $\times 10^{-4}$. In Figure 1, we show the quadrupole PSF anisotropy fields as measured from stellar ellipticities before and after the anisotropic PSF correction for our target clusters. Figure 2 shows the distributions of stellar ellipticity components before and after the PSF anisotropy correction. In addition, we adopt a conservative magnitude limit $m < 25.5$–26.0 AB mag, depending on the depth of the data for each cluster, to avoid systematic errors in the shape measurement (see Umetsu & Broadhurst 2008). From the rest of the object catalog, we select objects with $r_h > \overline{r^*_h} + \sigma(r^*_h)$ pixels as a magnitude-selected weak-lensing galaxy sample, where $\overline{r^*_h}$ is the median value of stellar half-light radii r^*_h, corresponding to half the median width of the circularized PSF over the data field, and $\sigma(r^*_h)$ is the rms dispersion of r^*_h.

Second, we need to correct image ellipticities for the isotropic smearing effect caused by atmospheric seeing and the window function used for the shape measurements. The pre-seeing reduced shear g_α can be estimated from

$$g_\alpha = \left(P^{-1}_g\right)_{\alpha\beta} e'_\beta, \tag{19}$$

with the *pre-seeing shear polarizability* tensor $P^g_{\alpha\beta}$ defined as (Hoekstra et al. 1998)

$$P^g_{\alpha\beta} = P^{\rm sh}_{\alpha\beta} - [P^{\rm sm}(P^{\rm sm*})^{-1} P^{\rm sh*}]_{\alpha\beta} \approx P^{\rm sh}_{\alpha\beta} - P^{\rm sm}_{\alpha\beta} \frac{{\rm tr}[P^{\rm sh*}]}{{\rm tr}[P^{\rm sm*}]}, \tag{20}$$

with $P^{\rm sh}$ being the *shear polarizability* tensor. In the second equality, we have used a trace approximation to the stellar shape tensors, $P^{\rm sh*}$ and $P^{\rm sm*}$. To apply Equation (19), the quantity ${\rm tr}[P^{\rm sh*}]/{\rm tr}[P^{\rm sm*}]$ must be known for each of the galaxies with different size scales. Following Hoekstra et al. (1998), we recompute the stellar shapes $P^{\rm sh*}$ and $P^{\rm sm*}$ in a range of filter scales r_g spanning that of the galaxy sizes ($r_g = [1, 10]$ pixels). At each filter scale r_g, the median $\langle {\rm tr}[P^{\rm sh*}]/{\rm tr}[P^{\rm sm*}]\rangle$ over the stellar sample is calculated, and used in Equation (20) as an estimate of ${\rm tr}[P^{\rm sh*}]/{\rm tr}[P^{\rm sm*}]$. Further, we adopt a scalar correction scheme, namely (Erben et al. 2001; Hoekstra et al. 1998; Umetsu & Broadhurst 2008),

$$(P_g)_{\alpha\beta} = \tfrac{1}{2}{\rm tr}[P_g]\delta_{\alpha\beta} \equiv P^{\rm s}_g \delta_{\alpha\beta}. \tag{21}$$

In order to suppress artificial effects due to the noisy $P^{\rm s}_g$ estimated for individual galaxies, we apply filtering to raw $P^{\rm s}_g$ measurements. We compute for each object a median value of $P^{\rm s}_g$ among N neighbors in the size and magnitude plane to define the object parameter space: firstly, for each object, N neighbors with raw $P^{\rm s}_g > 0$ are identified in the size (r_g) and magnitude plane; the median value of $P^{\rm s}_g$ is then used as the smoothed $P^{\rm s}_g$ for the object, $\langle P^{\rm s}_g\rangle$, and the variance σ^2_g of $g = g_1 + ig_2$ is calculated using Equation (19). The dispersion σ_g is used as an rms error of the shear estimate for individual galaxies. We take $N = 30$. Finally, we use the estimator $g_\alpha = e'_\alpha/\langle P^{\rm s}_g\rangle$ for the reduced shear.

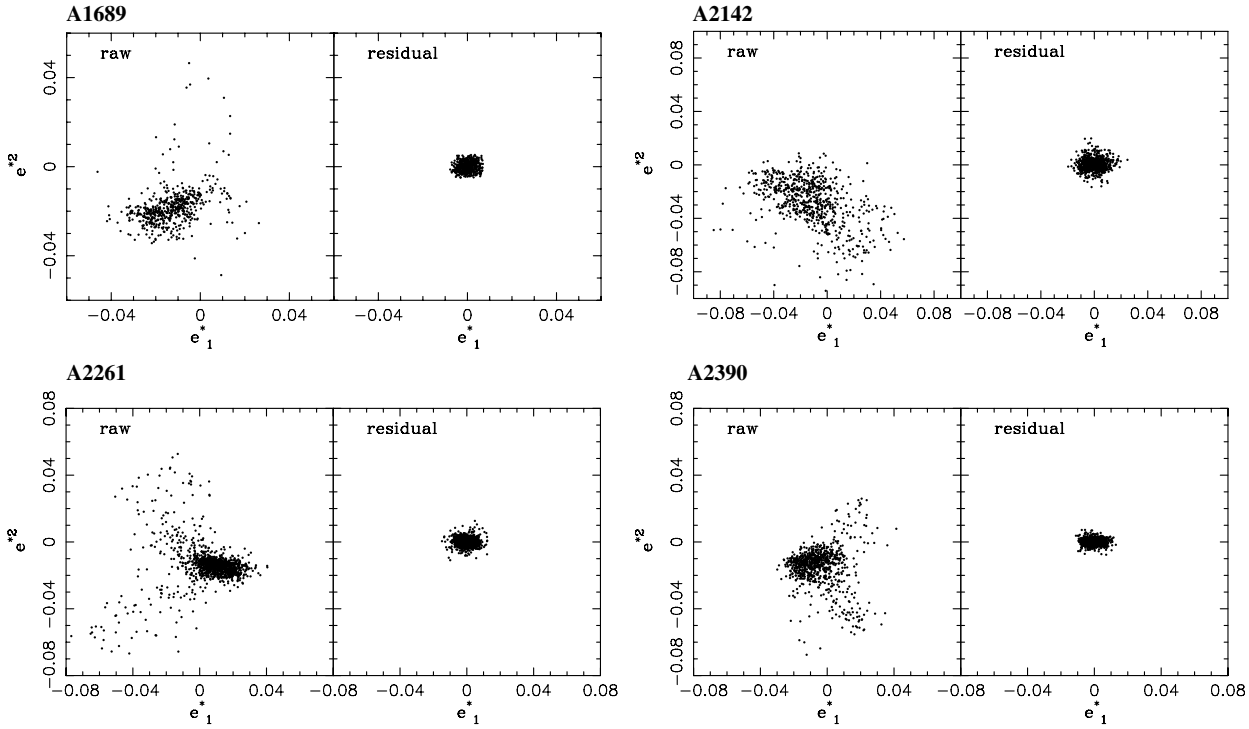

Figure 2. Stellar ellipticity distributions before and after the PSF anisotropy correction for individual clusters. For each cluster field, the left panel shows the raw ellipticity components (e_1^*, e_2^*) of stellar objects, and the right panel shows the residual ellipticity components $(\delta e_1^*, \delta e_2^*)$ after the PSF anisotropy correction.

4.3. Background Selection

It is crucial in the weak-lensing analysis to make a secure selection of background galaxies in order to minimize contamination by *unlensed* cluster/foreground galaxies and hence to make an accurate determination of the cluster mass profile; otherwise dilution of the distortion signal arises from the inclusion of unlensed galaxies, particularly at small radius where the cluster is relatively dense (Broadhurst et al. 2005a; Medezinski et al. 2007). This dilution effect is simply to reduce the strength of the lensing signal when averaged over a local ensemble of galaxies, in proportion to the fraction of unlensed galaxies whose orientations are randomly distributed, thus diluting the lensing signal relative to the reference background level derived from the background population (Medezinski et al. 2007).

To separate cluster members from the background and hence minimize the weak-lensing dilution, we follow an objective background selection method developed by Medezinski et al. (2007) and Umetsu & Broadhurst (2008). We select red galaxies with colors redder than the color–magnitude sequence of cluster E/S0 galaxies. The sequence forms a well defined line in object color–magnitude space due to the richness and relatively low redshifts of our clusters. These red galaxies are expected to lie in the background by virtue of k-corrections which are greater than for the red cluster sequence galaxies. This has been convincingly demonstrated spectroscopically by Rines & Geller (2008). We also include blue galaxies falling far from the cluster sequence to minimize cluster contamination.

Figure 3 shows for each cluster the mean distortion strength averaged over a wide radial range of $\theta = [1', 18']$ as a function of color limit, done separately for the blue (left) and red (right) samples, where the color boundaries for the present analysis are indicated by vertical dashed lines for respective color samples. Here, we do not apply area weighting to enhance the effect of dilution in the central region (see Umetsu & Broadhurst 2008). A sharp drop in the lensing signal is seen when the cluster red sequence starts to contribute significantly, thereby reducing the mean lensing signal. Note that the background populations do not need to be complete in any sense but should simply be well defined and contain only background. For A1689, the weak-lensing signal in the blue sample is systematically lower than that of the red sample, so that blue galaxies in A1689 are excluded from the present analysis, as was done in Umetsu & Broadhurst (2008); on the other hand, our improved color selection for the red sample has led to a $\sim 16\%$ increase of red galaxies. In the present study we use for A2142 the same Subaru images as analyzed by Okabe & Umetsu (2008), but we have improved significantly our lensing measurements by including blue, as well as red, galaxies, where the sample size has been increased by a factor of 4.

An estimate of the background depth is required when converting the observed lensing signal into physical mass units, because the lensing signal depends on the source redshifts in proportion to D_{ds}/D_s. The mean depth is sufficient for our purposes as the variation of the lens distance ratio, D_{ds}/D_s, is slow for our sample because the clusters are at relatively low redshifts ($z_d \sim 0.1$–0.2) compared to the redshift range of the background galaxies. We estimate the mean depth $\langle D_{ds}/D_s \rangle$ of the combined red+blue background galaxies by applying our color–magnitude selection to Subaru multicolor photometry of the HDF-N region (Capak et al. 2004) or the COSMOS deep field (Capak et al. 2007), depending on the availability of filters. The fractional uncertainty in the mean depth $\langle D_{ds}/D_s \rangle$ for the red galaxies is typically $\sim 3\%$, while it is about 5% for the blue galaxies. It is useful to define the distance-equivalent source redshift $z_{s,D}$ (Medezinski et al. 2007; Umetsu & Broadhurst 2008) defined as

$$\left\langle \frac{D_{ds}}{D_s} \right\rangle_{z_s} = \left. \frac{D_{ds}}{D_s} \right|_{z_s = z_{s,D}}. \tag{22}$$

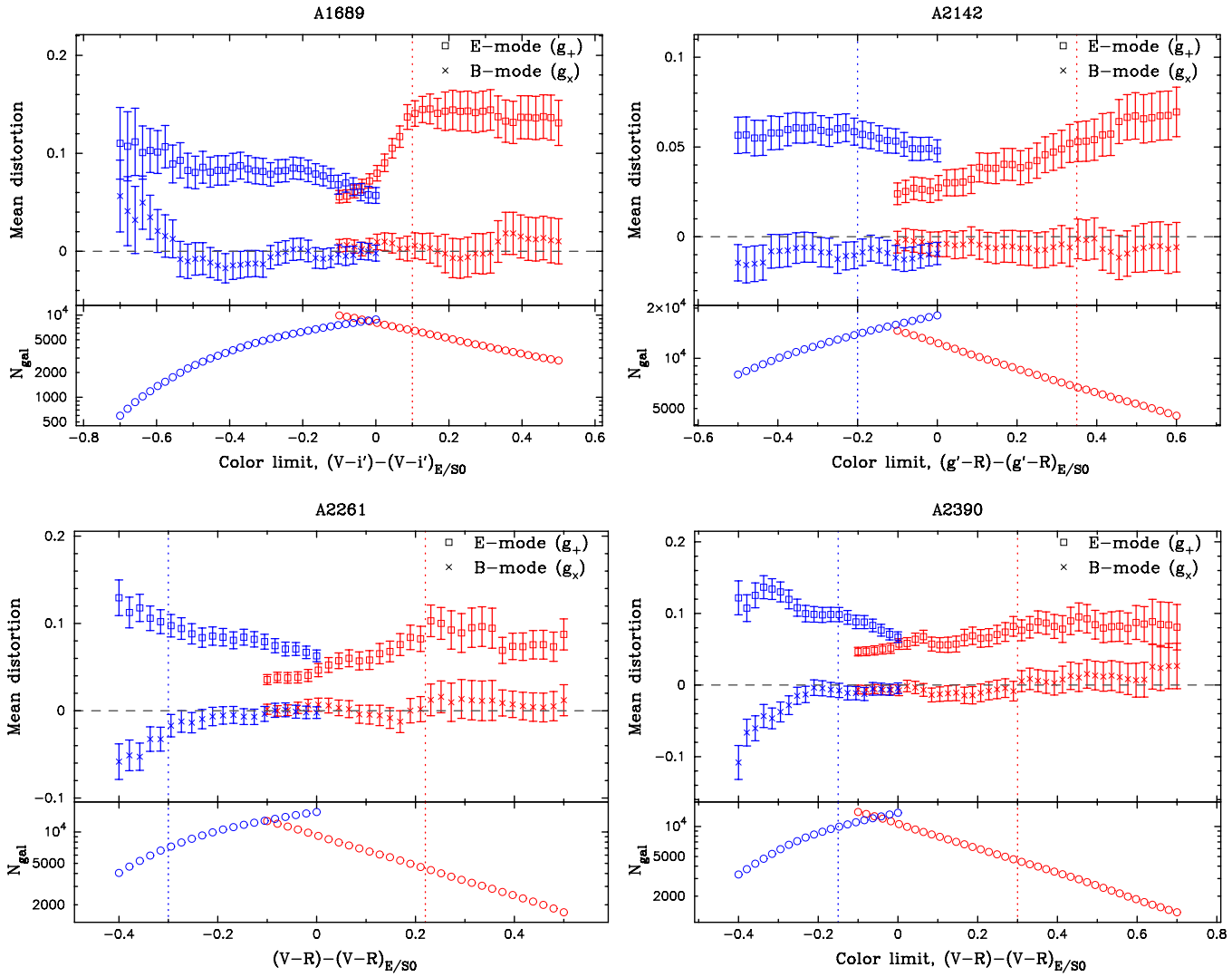

Figure 3. Top panels: mean shape distortions (g_+, $g_\times$) averaged over the entire cluster region ($1' < \theta < 18'$) for the four clusters done separately for the blue and red samples, in order to establish the boundaries of the color distribution free of cluster members. Bottom panels: respective numbers of galaxies as a function of color limit in the red (right) and the blue (blue) samples.

We find $z_{s,D} = 0.70^{+0.06}_{-0.05}$, $0.95^{+0.79}_{-0.30}$, $0.98^{+0.24}_{-0.16}$, and$1.00^{+0.25}_{-0.16}$ for A1689, A2142, A2261, and A2390, respectively. For the nearby cluster A2142 at $z \simeq 0.09$, a precise knowledge of the source redshift is not critical at all for lensing work. The mean surface number density (n_g) of the combined blue+red sample, the blue-to-red fraction of background galaxies (B/R), the estimated mean depth $\langle D_{ds}/D_s \rangle$, and the effective source redshift $z_{s,D}$ are listed in Table 2.

4.4. Weak-Lensing Map-Making

Weak-lensing measurements of the gravitational shear field can be used to reconstruct the underlying projected mass-density field. In the present study, we will use the dilution-free, color-selected background sample (Section 4.3) both for the two-dimensional mass reconstruction and the lens profile measurements.[16]

[16] Okabe & Umetsu (2008) used the magnitude-selected galaxy sample in their map-making of nearby merging clusters to increase the background sample size, while the dilution-free red background sample was used in their lensing mass measurements.

Firstly, we pixelize distortion data of background galaxies into a regular grid of pixels using a Gaussian $w_g(\theta) \propto \exp[-\theta^2/\theta_f^2]$ with $\theta_f = \mathrm{FWHM}/\sqrt{4\ln 2}$. Further we incorporate in the pixelization a statistical weight u_g for an individual galaxy, so that the smoothed estimate of the reduced shear field at an angular position $\boldsymbol{\theta}$ is written as

$$\bar{g}_\alpha(\boldsymbol{\theta}) = \frac{\sum_i w_g(\boldsymbol{\theta} - \boldsymbol{\theta}_i) u_{g,i} g_{\alpha,i}}{\sum_i w_g(\boldsymbol{\theta} - \boldsymbol{\theta}_i) u_{g,i}}, \tag{23}$$

where $g_{\alpha,i}$ is the reduced shear estimate of the ith galaxy at angular position $\boldsymbol{\theta}_i$, and $u_{g,i}$ is the statistical weight of the ith galaxy taken as the inverse variance, $u_{g,i} = 1/(\sigma_{g,i}^2 + \alpha^2)$, with $\sigma_{g,i}$ being the rms error for the shear estimate of the ith galaxy (see Section 4.2.2) and α^2 being the softening constant variance (Hamana et al. 2003). We choose $\alpha = 0.4$, which is a typical value of the mean rms $\bar{\sigma}_g$ over the background sample. The case with $\alpha = 0$ corresponds to an inverse-variance weighting. On the other hand, the limit $\alpha \gg \sigma_{g,i}$ yields a uniform weighting. We have confirmed that our results are insensitive to the choice of α (i.e., inverse-variance or uniform weighting) with the adopted smoothing parameters. The error

variance for the smoothed shear $\bar{g} = \bar{g}_1 + i\bar{g}_2$ (23) is then given as

$$\sigma^2_{\bar{g}}(\boldsymbol{\theta}) = \frac{\sum_i w^2_{g,i} u^2_{g,i} \sigma^2_{g,i}}{\left(\sum_i w_{g,i} u_{g,i}\right)^2}, \quad (24)$$

where $w_{g,i} = w_g(\boldsymbol{\theta} - \boldsymbol{\theta}_i)$ and we have used $\langle g_{\alpha,i}\, g_{\beta,j}\rangle = (1/2)\sigma^2_{g,i}\delta^{\rm K}_{\alpha\beta}\delta^{\rm K}_{ij}$ with $\delta^{\rm K}_{\alpha\beta}$ and $\delta^{\rm K}_{ij}$ being the Kronecker's delta.

We then invert the pixelized reduced-shear field (23) to obtain the lensing convergence field $\kappa(\boldsymbol{\theta})$ using Equation (12). In the map-making we assume linear shear in the weak-lensing limit, that is, $g_\alpha = \gamma_\alpha/(1-\kappa) \approx \gamma_\alpha$. We adopt the Kaiser & Squires inversion method (Kaiser & Squires 1993), which makes use of the two-dimensional Green function in an infinite space (Section 2.2). In the linear map-making process, the pixelized shear field is weighted by the inverse of the variance in Equation (24). Note that this weighting scheme corresponds to using only the diagonal part of the noise covariance matrix, $N(\boldsymbol{\theta}_i, \boldsymbol{\theta}_j) = \langle \overline{\Delta g}(\boldsymbol{\theta}_i)\overline{\Delta g}(\boldsymbol{\theta}_j)\rangle$, which is only an approximation of the actual inverse noise weighting in the presence of pixel-to-pixel correlation due to nonlocal Gaussian smoothing. In Table 2, we list the rms noise level in the reconstructed $\kappa(\boldsymbol{\theta})$ field for our sample of target clusters. For all of the clusters, the smoothing scale θ_f is taken to be $\theta_f = 1'$ ($\theta_{\rm FWHM} \simeq 1.'665$), which is larger than the Einstein radius for our background galaxies. Hence, our weak-lensing approximation here is valid in all clusters.

In Figure 4 we show, for the four clusters, two-dimensional maps of the lensing convergence $\kappa(\boldsymbol{\theta}) = \Sigma_m(\boldsymbol{\theta})/\Sigma_{\rm crit}$ reconstructed from the Subaru distortion data (Section 4.4), each with the corresponding gravitational shear field overlaid. Here, the resolution of the κ field is $\sim 1.'665$ in FWHM for all of the four clusters. The side length of the displayed region is $22'$, corresponding roughly to the instantaneous field of view of AMiBA ($\simeq 23'$ in FWHM). In the absence of higher order effects, weak lensing only induces curl-free E-mode distortions, responsible for tangential shear patterns, while the B-mode lensing signal is expected to vanish. For each case, a prominent mass peak is visible in the cluster center, around which the lensing distortion pattern is clearly tangential.

Also shown in Figure 4 are contours of the AMiBA flux density due to the thermal SZE obtained by Wu et al. (2009). The resolution of AMiBA7 is about $6'$ in FWHM (Section 3). The AMiBA map of A1689 reveals a bright and compact structure in the SZE, similar to the compact and round mass distribution reconstructed from the Subaru distortion data. A2142 shows an extended structure in the SZE elongated along the northwest–southeast direction, consistent with the direction of elongation of the X-ray halo, with its general cometary appearance (Markevitch et al. 2000). In addition, A2142 shows a slight excess in SZE signals located $\sim 10'$ northwest of the cluster center, associated with mass substructure seen in our lensing κ map (Figure 4). This slight excess SZE appears extended for a couple of synthesized beams, although the per-beam significance level is marginal (2σ–3σ). Okabe & Umetsu (2008) showed that this northwest mass substructure is also associated with a slight excess of cluster sequence galaxies, lying $\sim 5'$ ahead of the northwest edge of the central X-ray gas core. On the other hand, no X-ray counterpart to the northwest substructure was found in the X-ray images from *Chandra* and *XMM-Newton* observations (Okabe & Umetsu 2008). A2261 shows a filamentary mass structure with unknown redshift, extending to the west of the cluster core (Maughan et al. 2008), and likely background structures which coincide with redder galaxy concentrations (see Section 4.5.2 for details). Our AMiBA and Subaru observations show a compact structure both in mass and ICM. The elliptical mass distribution in A2390 agrees well with the shape seen by AMiBA in the thermal SZE, and is also consistent with other X-ray and strong-lensing work. A quantitative comparison between the AMiBA SZE and Subaru lensing maps will be given in Section 5.

4.5. Cluster Lensing Profiles

4.5.1. Lens Distortion

The spin-2 shape distortion of an object due to gravitational lensing is described by the complex reduced shear, $g = g_1 + ig_2$ (see Equation (15)), which is coordinate dependent. For a given reference point on the sky, one can instead form coordinate-independent quantities, the tangential distortion g_+ and the 45° rotated component, from linear combinations of the distortion coefficients g_1 and g_2 as

$$g_+ = -(g_1\cos 2\phi + g_2 \sin 2\phi), \quad g_\times = -(g_2\cos 2\phi - g_1 \sin 2\phi), \quad (25)$$

where ϕ is the position angle of an object with respect to the reference position, and the uncertainty in the g_+ and $g_\times$ measurement is $\sigma_+ = \sigma_\times = \sigma_g/\sqrt{2} \equiv \sigma$ in terms of the rms error σ_g for the complex shear measurement. In practice, the reference point is taken to be the cluster center, which is well determined by the locations of the brightest cluster galaxies. To improve the statistical significance of the distortion measurement, we calculate the weighted average of g_+ and $g_\times$, and its weighted error, as

$$\langle g_+(\theta_m)\rangle = \frac{\sum_i u_{g,i}\, g_{+,i}}{\sum_i u_{g,i}}, \quad (26)$$

$$\langle g_\times(\theta_m)\rangle = \frac{\sum_i u_{g,i}\, g_{\times,i}}{\sum_i u_{g,i}}, \quad (27)$$

$$\sigma_+(\theta_m) = \sigma_\times(\theta_m) = \sqrt{\frac{\sum_i u^2_{g,i}\sigma^2_i}{\left(\sum_i u_{g,i}\right)^2}}, \quad (28)$$

where the index i runs over all of the objects located within the mth annulus with a median radius of θ_m, and $u_{g,i}$ is the inverse-variance weight for the ith object, $u_{g,i} = 1/(\sigma^2_{g,i} + \alpha^2)$, softened with $\alpha = 0.4$ (see Section 4.4).

Now we assess cluster lens-distortion profiles from the color-selected background galaxies (Section 4.3) for the four clusters, in order to examine the form of the underlying cluster mass profile and to characterize cluster mass properties. In the weak-lensing limit ($\kappa, |\gamma| \ll 1$), the azimuthally averaged tangential distortion profile $\langle g_+(\theta)\rangle$ (Equation (26)) is related to the projected mass-density profile (e.g., Bartelmann & Schneider 2001) as

$$\langle g_+(\theta)\rangle \simeq \langle \gamma_+(\theta)\rangle = \bar{\kappa}(<\theta) - \langle\kappa(\theta)\rangle, \quad (29)$$

where $\langle\cdots\rangle$ denotes the azimuthal average, and $\bar{\kappa}(<\theta)$ is the mean convergence within a circular aperture of radius θ defined as $\bar{\kappa}(<\theta) = (\pi\theta^2)^{-1}\int_{|\boldsymbol{\theta}'|\leqslant\theta} d^2\theta'\,\kappa(\boldsymbol{\theta}')$. Note that Equation (29) holds for an arbitrary mass distribution. With the assumption of quasi-circular symmetry in the projected mass distribution, one can express the tangential distortion as $\langle g_+(\theta)\rangle \simeq [\bar{\kappa}(<\theta) - \langle\kappa(\theta)\rangle]/[1 - \langle\kappa(\theta)\rangle]$ in the nonlinear but subcritical ($\det \mathcal{A}(\boldsymbol{\theta}) > 0$) regime.

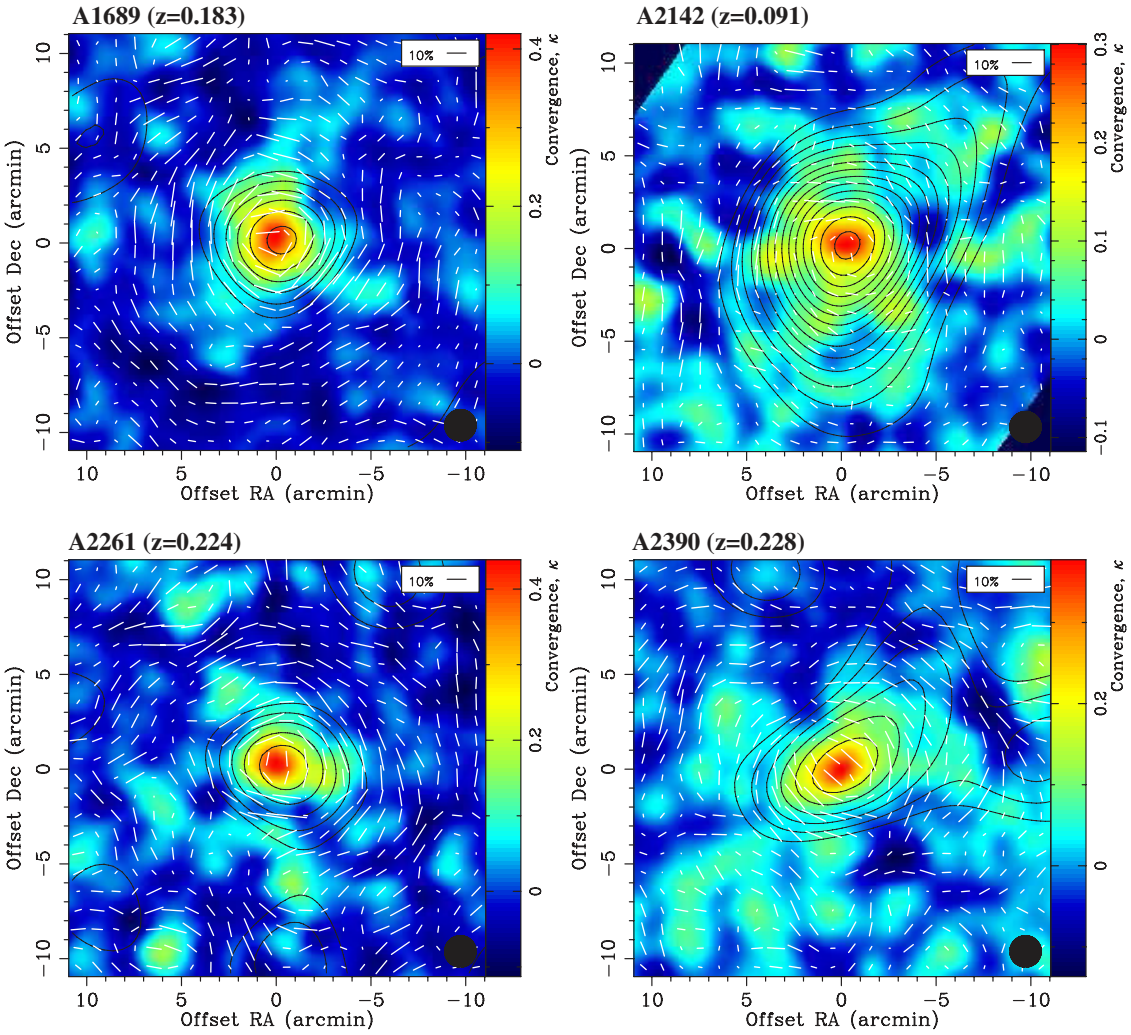

Figure 4. Mass maps of the central 22′ × 22′ of four AMiBA/Subaru clusters reconstructed from Subaru weak-lensing data, with the gravitational shear field of background galaxies overlaid; 10% ellipticity is indicated in top right panel, and the resolution characterized by Gaussian FWHM is shown in bottom right panel. Also overlaid are contours of the SZE flux densities at 94 GHz, observed with the seven-element AMiBA, given in units of 1σ reconstruction error. The resolution of AMiBA, given in Gaussian FWHM, is 6′. For all four clusters the distribution of the SZE signal is well correlated with the projected mass distribution, indicating that the hot gas in the clusters traces well the underlying gravitational potential dominated by unseen DM. The dark blue regions in the mass map of A2142 are outside the Subaru observations.

Figure 5 shows the azimuthally averaged radial profiles of the tangential distortion, $\langle g_+ \rangle$ (E mode), and the 45° rotated component, $\langle g_\times \rangle$ (B mode). Here the presence of B modes can be used to check for systematic errors. For each of the clusters, the observed E-mode signal is significant at the 12–16σ level out to the limit of our data ($\theta \sim 20'$). The significance level of the B-mode detection is about 2.5σ for each cluster, which is about a factor of 5 smaller than E-mode.

The measured g_+ profiles are compared with two representative cluster mass models, namely the NFW model and the singular isothermal sphere (SIS) model. Firstly, the NFW universal density profile has a two-parameter functional form as

$$\rho_{\rm NFW}(r) = \frac{\rho_s}{(r/r_s)(1+r/r_s)^2}, \tag{30}$$

where ρ_s is a characteristic inner density and r_s is a characteristic inner radius. The logarithmic gradient $n \equiv d\ln\rho(r)/d\ln r$ of the NFW density profile flattens continuously toward the center of mass, with a flatter central slope $n = -1$ and a steeper outer slope ($n \to$-3 when $r \to \infty$) than a purely isothermal structure ($n = -2$). A useful index, the concentration, compares the virial radius, $r_{\rm vir}$, to r_s of the NFW profile, $c_{\rm vir} = r_{\rm vir}/r_s$. We specify the NFW model with the halo virial mass $M_{\rm vir}$ and the concentration $c_{\rm vir}$ instead of ρ_s and r_s.[17] We employ the radial dependence of the NFW lensing profiles, $\kappa_{\rm NFW}(\theta)$ and $\gamma_{+,\rm NFW}(\theta)$, given by Bartelmann (1996) and Wright & Brainerd (2000). Next, the SIS density profile is given by

$$\rho_{\rm SIS}(r) = \frac{\sigma_v^2}{2\pi G r^2}, \tag{31}$$

where σ_v is the one-dimensional isothermal velocity dispersion of the SIS halo. The lensing profiles for the SIS model, obtained by projections of the three-dimensional mass distribution, are found to be

$$\kappa_{\rm SIS}(\theta) = \gamma_{+,\rm SIS}(\theta) = \frac{\theta_E}{2\theta}, \tag{32}$$

where θ_E is the Einstein radius defined by $\theta_E \equiv 4\pi(\sigma_v/c)^2 D_{ds}/D_s$.

[17] We assume that the cluster redshift z_d is equal to the cluster virial redshift.

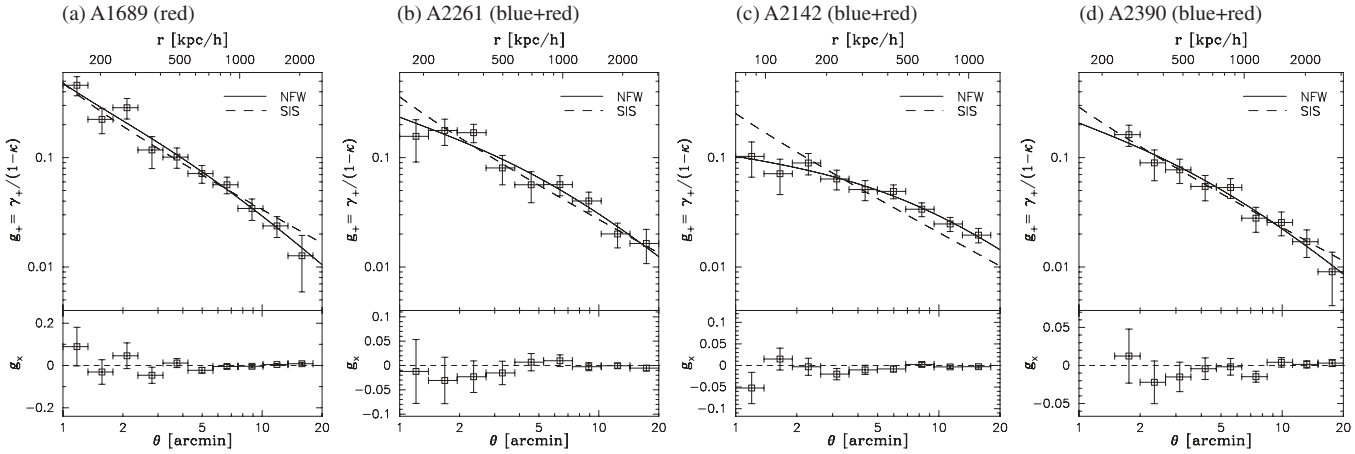

Figure 5. Azimuthally averaged radial profiles of the tangential reduced shear g_+ (upper panels) for the four clusters based on the combined red and blue background samples. The solid and dashed curves show the best-fitting NFW and SIS profiles for each cluster. Shown below is the 45° rotated (×) component, $g_\times$.

Table 3
Summary of Best-Fit Mass Models From Subaru Distortion Data

Cluster	Tangential Reduced Shear, g_+							Lensing Convergence, κ			
	SIS			NFW				NFW			
	σ_v (kms^{-1})	χ^2/dof	θ_E ($''$)	M_{vir} ($10^{15}\,M_\odot h^{-1}$)	c_{vir}	χ^2/dof	θ_E ($''$)	M_{vir} ($10^{15}\,M_\odot h^{-1}$)	c_{vir}	χ^2/dof	θ_E ($''$)
A1689	1403 ± 41	11/9	47 ± 3	$1.09^{+0.18}_{-0.16}$	$15.6^{+4.8}_{-3.3}$	7.3/8	47^{+15}_{-14}	$1.05^{+0.18}_{-0.15}$	$15.8^{+14.2}_{-8.0}$	5.3/8	46^{+26}_{-31}
A2142	970 ± 27	39/8	25 ± 1	$1.07^{+0.22}_{-0.16}$	$5.6^{+0.9}_{-0.8}$	2.1/7	$1.2^{+2.9}_{-0.9}$	$1.06^{+0.19}_{-0.16}$	$4.9^{+1.2}_{-1.0}$	20/10	$0.5^{+2.3}_{-0.4}$
A2261	1276 ± 43	8.7/8	37 ± 3	$1.35^{+0.26}_{-0.22}$	$6.4^{+1.9}_{-1.4}$	7.7/7	20^{+16}_{-11}	$1.26^{+0.20}_{-0.17}$	$10.2^{+7.1}_{-3.5}$	9.8/8	37^{+25}_{-19}
A2390	1139 ± 38	3.8/8	30 ± 2	$0.90^{+0.15}_{-0.14}$	$6.9^{+2.3}_{-1.5}$	3.8/7	15^{+13}_{-8}	$0.92^{+0.15}_{-0.12}$	$7.3^{+6.9}_{-2.9}$	8.1/8	17^{+26}_{-14}

Notes. A flat prior of $c_{vir} \leqslant 30$ is assumed for the halo concentration of the NFW model. The Einstein radius θ_E is calculated for a background source at $z_s = 1.5$, corresponding roughly to the mean depth of blue+red background galaxies.

Table 3 lists the best-fitting parameters for these models, together with the predicted Einstein radius θ_E for a fiducial source at $z_s = 1.5$, corresponding roughly to the median redshifts of our blue background galaxies. For a quantitative comparison of the models, we introduce as a measure of the *goodness of fit* the significance probability $Q(\nu/2, \chi^2/2)$ to find by chance a value of χ^2 as poor as the observed value for a given number of dof, ν (see Section 15.2 in Press et al. 1992).[18] We find with our best-fit NFW models Q-values of $Q \simeq 0.50, 0.95, 0.36$, and 0.80, and with our best-fit SIS models $Q \simeq 0.28, 5.0 \times 10^{-6}, 0.37$, and 0.87, for A1689, A2142, A2261, and A2390, respectively. Both models provide statistically acceptable fits for A1689, A2261, and A2390. For our lowest z cluster A2142, the curvature in the g_+ profile is pronounced, and an SIS model for A2142 is strongly ruled out by the Subaru distortion data alone, where the minimum χ^2 is $\chi^2_{min} = 39$ with 8 dof.

4.5.2. Lens Convergence

Although the lensing distortion is directly observable, the effect of substructure on the gravitational shear is nonlocal. Here, we examine the lens convergence (κ) profiles using the shear-based one-dimensional reconstruction method developed by Umetsu & Broadhurst (2008). See Appendix A.1 for details of the reconstruction method.

In Figure 6 we show, for the four clusters, model-independent κ profiles derived using the shear-based one-dimensional reconstruction method, together with predictions from the best-fit NFW models for the $\kappa(\theta)$ and $g_+(\theta)$ data. The substructure contribution to $\kappa(\theta)$ is local, whereas the inversion from the observable distortion to κ involves a nonlocal process. Consequently, the one-dimensional inversion method requires a boundary condition specified in terms of the mean κ value within an outer annular region (lying out to 18′–19′). We determine this value for each cluster using the best-fit NFW model for the g_+ profile (Table 3).

We find that the two sets of best-fit NFW parameters are in excellent agreement for all except A2261: for A2261, the best-fit values of c_{vir} from the g_+ and κ profiles are in poorer agreement. In Figures 4 and 6 we see that the NFW fit to the g_+ profile of A2261 is affected by the presence of mass structures at outer radii, $\theta \simeq 4'$ and 10′, resulting in a slightly shallower profile ($c_{vir} \simeq 6.4$) than in the κ analysis. It turns out that these mass structures are associated with galaxy overdensities whose mean colors are redder than the cluster sequence for A2261 at $z = 0.224$, $\Delta(V - R_c) \equiv (V - R_c) - (V - R_c)_{A2261} \sim +0.6$, and hence they are likely to be physically unassociated background objects. The NFW fit to $\kappa(\theta)$ yields a steeper profile with a high concentration, $c_{vir} \simeq 10.2$, which implies a large Einstein angle of $\theta_E \simeq 37''$ at $z_s = 1.5$ (Table 3). This is in good agreement with our preliminary strong-lensing model (A. Zitrin et al. 2009, in preparation) based on the method by Broadhurst et al. (2005b), in which the deflection field is constructed based on the smoothed cluster light distribution to predict the appearance

[18] Note that a Q-value greater than 0.1 indicates a satisfactory agreement between the data and the model; if $Q \gtrsim 0.001$, the fit may be acceptable, e.g., in a case that the measurement errors are moderately underestimated; if $Q \lesssim 0.001$, the model may be called into question.

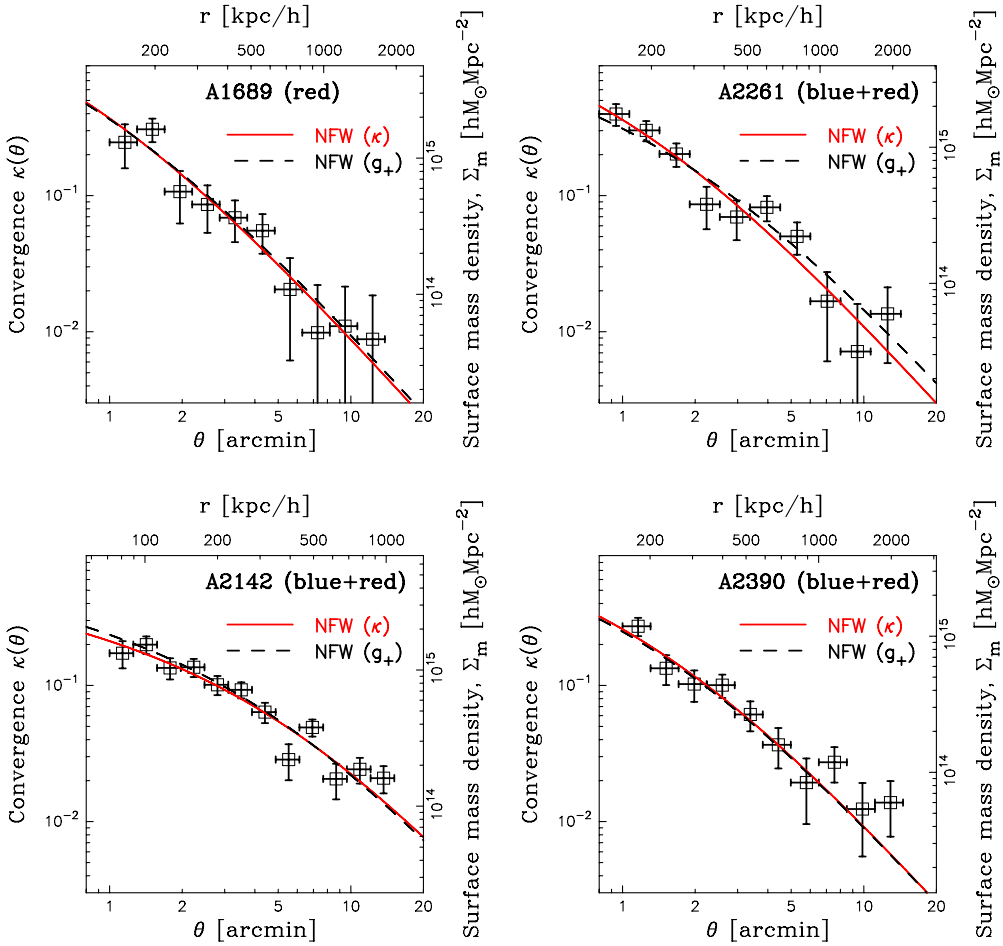

Figure 6. Model-independent radial profiles of the lensing convergence $\kappa(\theta) = \Sigma_m(\theta)/\Sigma_{\rm crit}$ for the four clusters derived from a variant of the nonlinear aperture mass densitometry. For each cluster, the best-fitting NFW model for the κ profile is shown with a solid line. The dashed curve shows the best-fitting NFW model for the g_+ profile in Figure 5.

and positions of counter images of background galaxies. This model is refined as new multiply lensed images are identified in deep Subaru VR_c and CFHT/WIRCam JHK_s images, and incorporated to improve the cluster mass model. Figure 7 shows the tangential critical curve predicted for a background source at $z_s \sim 1.5$, overlaid on the Subaru $V + R_c$ pseudo-color image in the central $6.'7 \times 6.'7$ region of A2261. The predicted critical curve is a nearly circular Einstein ring, characterized by an effective radius of $\theta_{\rm E} \sim 40''$ (see Oguri & Blandford 2009). This motivates us to further improve the statistical constraints on the NFW model by combining the outer lens convergence profile with the observed constraint on the inner Einstein radius. A joint fit of the NFW profile to the κ profile and the inner Einstein-radius constraint with $\theta_{\rm E} = 40'' \pm 4''$ ($z_s = 1$) tightens the constraints on the NFW parameters (see Section 5.4.2 of Umetsu & Broadhurst 2008): $M_{\rm vir} = 1.25^{+0.17}_{-0.16} \times 10^{15}\, M_\odot\, h^{-1}$ and $c_{\rm vir} = 11.1^{+2.2}_{-1.9}$. This model yields an Einstein radius of $\theta_E = (40 \pm 11)''$ at $z_s = 1.5$. In the following analysis, we will adopt this as our primary mass model of A2261.

For the strong-lensing cluster A1689, more detailed lensing constraints are available from joint observations with the high-resolution *Hubble Space Telescope* (*HST*) Advanced Camera for Surveys (ACS) and the wide-field Subaru/Suprime-Cam (Broadhurst et al. 2005a; Umetsu & Broadhurst 2008). In Umetsu & Broadhurst (2008), we combined all possible lensing measurements, namely, the ACS strong-lensing profile of Broadhurst et al. (2005a) and Subaru weak-lensing distortion and magnification data, in a full two-dimensional treatment, to achieve the maximum possible lensing precision. Note that the combination of distortion and magnification data breaks the mass-sheet degeneracy (see Equation (16)) inherent in all reconstruction methods based on distortion information alone (Bartelmann et al. 1996). It was found that the joint ACS and Subaru data, covering a wide range of radii from 10 up to 2000 kpc h^{-1}, are well approximated by a single NFW profile with $M_{\rm vir} = (1.5 \pm 0.1^{+0.6}_{-0.3}) \times 10^{15}\, M_\odot\, h^{-1}$ and $c_{\rm vir} = 12.7 \pm 1 \pm 2.8$ (statistical uncertainty followed by systematic uncertainty at 68% confidence).[19] This properly reproduces the Einstein radius, which is tightly constrained by detailed strong-lens modeling (Broadhurst et al. 2005b; Halkola et al. 2006; Limousin et al. 2007): $\theta_{\rm E} \simeq 52''$ at $z_s = 3.05$ (or $\theta_{\rm E} \simeq 45''$ at a fiducial source redshift of $z_s = 1$). With the improved color selection for the red background sample (see Section 4.3), we have redone a joint fit to the ACS and Subaru lensing observations using the two-dimensional method of Umetsu & Broadhurst (2008): the refined constraints on the NFW parameters are $M_{\rm vir} = 1.55^{+0.13}_{-0.12} \times 10^{15}\, M_\odot\, h^{-1}$ and $c_{\rm vir} = 12.3^{+0.9}_{-0.8}$, yielding an Einstein radius of $50^{+6.5}_{-6.0}$ arcsec at $z_s = 1.5$. In the

[19] In Umetsu & Broadhurst (2008), cluster masses are expressed in units of $10^{15} M_\odot$ with $h = 0.7$. The systematic uncertainty in $M_{\rm vir}$ is tightly correlated with that in $c_{\rm vir}$ through the Einstein-radius constraint by the ACS observations.

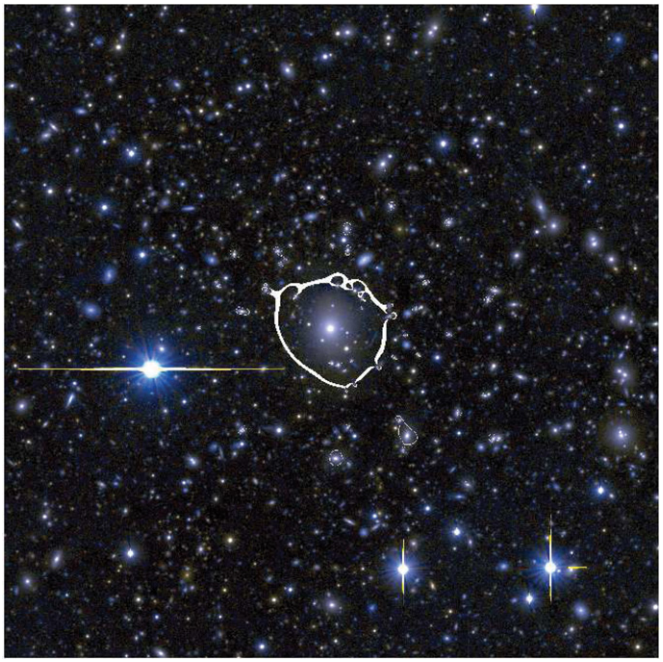

Figure 7. Subaru $V + R_c$ pseudo-color image of the central $6.'7 \times 6.'7$ (2 K pixels $\times$ 2 K pixels) region of the cluster A2261 at $z_d = 0.226$. Overlaid is the tangential critical curve predicted for a background source at $z_s \sim 1.5$ based on strong-lensing modeling of multiply lensed images and tangential arcs registered in deep Subaru VR_c and CFHT/WIRCam JHK_S images. The effective radius of the tangential critical curve defines the Einstein radius, $\theta_E \approx 40'$, at $z_s \sim 1.5$.

following, we will adopt this refined NFW profile as our primary mass model of A1689.

5. DISTRIBUTIONS OF MASS AND HOT BARYONS

Here, we aim to compare the projected distribution of mass and ICM in the clusters using our Subaru weak-lensing and AMiBA SZE maps. To make a quantitative comparison, we first define the "cluster shapes" on weak-lensing mass structure by introducing a spin-2 halo ellipticity $e^{\rm halo} = e_1^{\rm halo} + i e_2^{\rm halo}$, defined in terms of weighted quadrupole shape moments $Q_{\alpha\beta}^{\rm halo}$ ($\alpha, \beta = 1, 2$) as

$$e_\alpha^{\rm halo}(\theta_{\rm ap}) = \left(\frac{Q_{11}^{\rm halo} - Q_{22}^{\rm halo}}{Q_{11}^{\rm halo} + Q_{22}^{\rm halo}}, \frac{2Q_{12}^{\rm halo}}{Q_{11}^{\rm halo} + Q_{22}^{\rm halo}} \right), \quad (33)$$

$$Q_{\alpha\beta}^{\rm halo}(\theta_{\rm ap}) = \int_{\Delta\theta \leqslant \theta_{\rm ap}} d^2\theta \, \Delta\theta_\alpha \Delta\theta_\beta \, \kappa(\boldsymbol{\theta}), \quad (34)$$

where $\theta_{\rm ap}$ is the circular aperture radius and $\Delta\theta_\alpha$ is the angular displacement vector from the cluster center. Similarly, the spin-2 halo ellipticity for the SZE is defined using the cleaned SZE decrement map $-\Delta I(\boldsymbol{\theta}) \propto y(\boldsymbol{\theta})$ instead of $\kappa(\boldsymbol{\theta})$ in Equation (34). The degree of halo ellipticity is quantified by the modulus of the spin-2 ellipticity, $|e^{\rm halo}| = \sqrt{(e_1^{\rm halo})^2 + (e_2^{\rm halo})^2}$, and the orientation of halo is defined by the position angle of the major axis, $\phi^{\rm halo} = \arctan(e_2^{\rm halo}/e_1^{\rm halo})/2$. In order to avoid noisy shape measurements, we introduce a lower limit of $\kappa(\boldsymbol{\theta}) > 0$ and $-\Delta I(\boldsymbol{\theta}) > 0$ in Equation (34). Practical shape measurements are done using pixelized lensing and SZE maps shown in Figure 4. The images are sufficiently oversampled that the integral in Equation (34) can be approximated by the discrete sum. Note that a comparison in terms of the shape parameters is optimal for the present case where the paired AMiBA and weak-lensing images have different angular resolutions: $\theta_{\rm FWHM} \simeq 6'$ FWHM for AMiBA7 and $\theta_{\rm FWHM} \simeq 1.'7$ FWHM for Subaru weak lensing. When the aperture diameter is larger than the resolution $\theta_{\rm FWHM}$, i.e., $\theta_{\rm ap} > \theta_{\rm FWHM}/2$, the halo shape parameters can be reasonably defined and measured from the maps.

Now we measure as a function of aperture radius $\theta_{\rm ap}$ the cluster ellipticity and orientation profiles for projected mass and ICM pressure as represented by the lensing κ and SZE decrement maps, respectively. For the Subaru weak lensing, the shape parameters are measured at $\theta_{\rm ap} = [1, 2, 3, \ldots, 11] \times \theta_{\rm FWHM}$ ($1.'7 \lesssim \theta_{\rm ap} \lesssim 18.'3$); for the AMiBA SZE, $\theta_{\rm ap} = [1, 2, 3] \times \theta_{\rm FWHM}$ ($6' \lesssim \theta_{\rm ap} \lesssim 18'$). The level of uncertainty in the halo shape parameters is assessed by a Monte Carlo error analysis assuming Gaussian errors for weak-lensing distortion and AMiBA visibility measurements (for the Gaussianity of AMiBA data see Nishioka et al. 2009). For each cluster and data set, we generate a set of 500 Monte Carlo simulations of Gaussian noise and propagate into final uncertainties in the spin-2 halo ellipticity, $e^{\rm halo}$. Figure 8 displays, for the four clusters, the resulting cluster ellipticity and orientation profiles on mass and ICM structure as measured from the Subaru weak-lensing and AMiBA SZE maps, shown separately for the ellipticity modulus $|e^{\rm halo}|$ and the orientation, $2\phi^{\rm halo}$ (twice the position angle). Overall, a good agreement is found between the shapes of mass and ICM structure up to large radii, in terms of both ellipticity and orientation. In particular, our results on A2142 and A2390 show that the mass and pressure distributions trace each other well at all radii. At a large radius of $\theta_{\rm ap} \gtrsim 10'$, the position angle of A2142 is $\phi^{\rm halo} \sim 50^\circ$. For A2390, the position angle is $\phi^{\rm halo} \sim 30^\circ$ at all radii.

6. CLUSTER GAS MASS FRACTION PROFILES

6.1. Method

In modeling the clusters, we consider two representative analytic models for describing the cluster DM and ICM distributions, namely (1) the Komatsu & Seljak (2001, hereafter KS01) model of the universal gas density/temperature profiles and (2) the isothermal β model, where both are physically motivated under the hypothesis of hydrostatic equilibrium and polytropic equation of state, $P \propto \rho^\gamma$, with an additional assumption about the spherical symmetry of the system.

Joint AMiBA SZE and Subaru weak-lensing observations probe cluster structures on angular scales up to $\Delta\theta \sim 23'$.[20] At the median redshift $\bar{z} \simeq 0.2$ of our clusters, this maximum angle covered by the data corresponds roughly to $r_{200} \approx 0.8 r_{\rm vir}$, except $r_{500} \approx 0.5 r_{\rm vir}$ for A2142 at $z = 0.09$. In order to better constrain the gas mass fraction in the outer parts of the clusters, we adopt a prior that the gas density profile $\rho_{\rm gas}(r)$ traces the underlying (total) mass–density profile, $\rho_{\rm tot}(r)$. Such a relationship is expected at large radii, where nongravitational processes, such as radiative cooling and star formation, have not had a major effect on the structure of the atmosphere so that the polytropic assumption remains valid (Lewis et al. 2000). Clearly this results in the gas mass fraction, $\rho_{\rm gas}(r)/\rho_{\rm tot}(r)$, tending to a constant at large radius. In the context of the isothermal β model, this simply means that $\beta = 2/3$.

In both models, for each cluster, the mass-density profile $\rho_{\rm tot}(r)$ is constrained solely by the Subaru weak-lensing data

[20] The FWHM of the primary beam pattern of the AMiBA is about $23'$, while the field of view of the Subaru/Suprime-Cam is about $34'$.

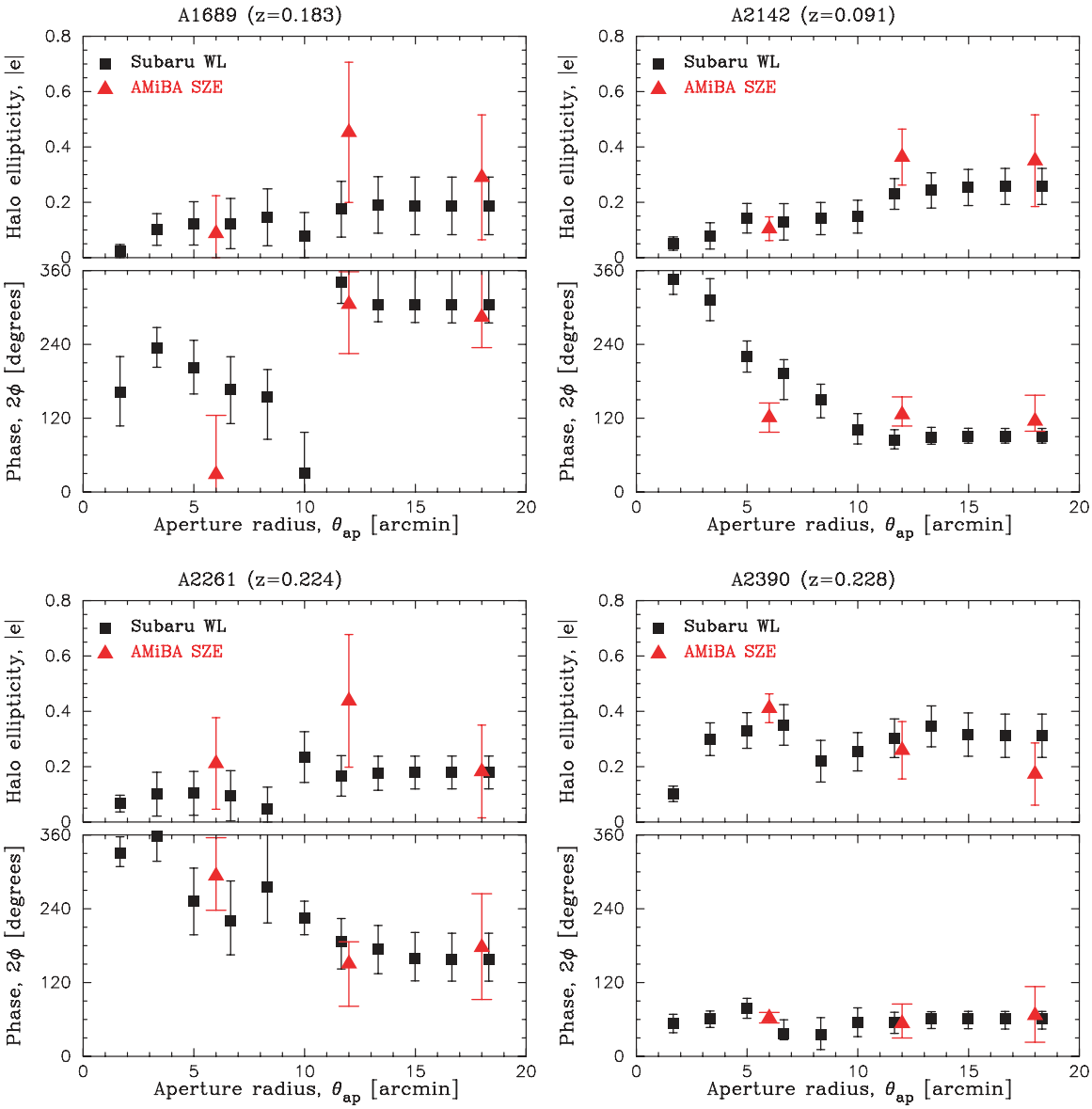

Figure 8. Cluster ellipticity and orientation profiles on mass and ICM structure as a function of aperture radius $\theta_{\rm ap}$, measured from the Subaru weak-lensing and AMiBA SZE maps shown in Figure 4. For each cluster, the top panel shows the halo ellipticity profile $|e^{\rm halo}|(\theta_{\rm ap})$, and the bottom panel shows the orientation profile $2\phi(\theta_{\rm ap})$, where $\phi^{\rm halo}$ represents the position angle of the major axis as measured from weighted quadrupole shape moments.

(Section 4), the gas temperature profile $T_{\rm gas}(r)$ is normalized by the spatially averaged X-ray temperature (see Table 1), and the electron pressure profile $P_e(r) = n_e(r)k_BT_e(r)$ is normalized by the AMiBA SZE data, where $n_e(r)$ is the electron number density and $T_e(r) = T_{\rm gas}(r)$ is the electron temperature. The gas density is then given by $\rho_{\rm gas}(r) = \mu_e m_p n_e(r)$.

6.2. Cluster Models

6.2.1. NFW-consistent Model of Komatsu & Seljak (2001)

The KS01 model describes the polytropic gas in hydrostatic equilibrium with a gravitational potential described by the *universal* density profile for collisionless CDM halos proposed by Navarro et al. (1996, hereafter NFW). See KS01, Komatsu & Seljak (2002, hereafter KS02), and Worrall & Birkinshaw (2006) for more detailed discussions. High-mass clusters with virial masses $M_{\rm vir} \gtrsim 10^{15}\,M_\odot\,h^{-1}$ are so massive that the virial temperature of the gas is too high for efficient cooling and hence the cluster potential simply reflects the dominant DM. This has been recently established by our Subaru weak-lensing study of several massive clusters (Broadhurst et al. 2005a, 2008; Umetsu & Broadhurst 2008).

In this model, the gas mass profile traces the NFW profile in the outer region of the halo ($r_{\rm vir}/2 \lesssim r \lesssim r_{\rm vir}$; see KS01), satisfying the adopted prior of the constant gas mass fraction $\rho_{\rm gas}(r)/\rho_{\rm tot}(r)$ at large radii. This behavior is supported by cosmological hydrodynamic simulations (e.g., Yoshikawa et al. 2000), and is recently found from the stacked SZE analysis of the *WMAP* three-year data (Atrio-Barandela et al. 2008). The shape of the gas distribution functions, as well as the polytropic index $\gamma_{\rm gas}$, can be fully specified by the halo virial mass, $M_{\rm vir}$, and the halo concentration, $c_{\rm vir} = r_{\rm vir}/r_s$, of the NFW profile.

In the following, we use the form of the NFW profile to determine $r_{\rm vir}$, r_{200}, r_{500}, and r_{2500}. Table 4 summarizes the NFW model parameters derived from our lensing analysis for the four clusters (see Section 4.5). For each cluster, we also

Table 4
Cluster Mass Models for Gas Mass Fraction Measurements

Cluster	NFW Model		SIS Model	r_{2500}	r_{500}	r_{200}	$r_{\rm vir}$
	$M_{\rm vir}$ ($10^{15}\,M_\odot\,h^{-1}$)	$c_{\rm vir}$	σ_v (km s^{-1})	(Mpc h^{-1})	(Mpc h^{-1})	(Mpc h^{-1})	(Mpc h^{-1})
A1689[a]	$1.55^{+0.13}_{-0.12}$	$12.3^{+0.9}_{-0.8}$	1403 ± 41	0.57 ± 0.01	1.16 ± 0.02	1.70 ± 0.04	2.13 ± 0.05
A2142	$1.07^{+0.22}_{-0.16}$	$5.6^{+0.9}_{-0.8}$	970 ± 27	0.43 ± 0.02	0.99 ± 0.04	1.51 ± 0.07	1.98 ± 0.10
A2261[b]	$1.25^{+0.17}_{-0.16}$	$11.1^{+2.2}_{-1.9}$	1276 ± 43	0.52 ± 0.02	1.06 ± 0.04	1.56 ± 0.06	1.94 ± 0.07
A2390	$0.90^{+0.15}_{-0.14}$	$6.9^{+2.3}_{-1.5}$	1139 ± 38	0.42 ± 0.03	0.92 ± 0.04	1.38 ± 0.06	1.73 ± 0.07

Notes.
[a] The NFW model is constrained by a joint fit to ACS strong-lensing and Subaru distortion+magnification data, presented in Umetsu & Broadhurst (2008), but with our improved color selection of the red background sample for Subaru distortion measurements (Section 4.5.2).
[b] The NFW model is constrained by a joint fit to the inner Einstein-radius constraint and the outer Subaru κ profile (Section 4.5.2).

list the corresponding ($r_{2500}, r_{500}, r_{200}, r_{\rm vir}$). For calculating $\gamma_{\rm gas}$ and the normalization factor $\eta(0)$ for a structure constant (B in Equation (16) of KS02), we follow the fitting formulae given by KS02, which are valid for halo concentration, $1 < c_{\rm vir} < 25$ (see Table 4). For our clusters, $\gamma_{\rm gas}$ is in the range of 1.15–1.20. Following the prescription in KS01, we convert the X-ray cluster temperature T_X to the central gas temperature $T_{\rm gas}(0)$ of the KS01 model.

6.2.2. Isothermal β Profile

The isothermal β model provides an alternative consistent solution of the hydrostatic equilibrium equation (Hattori et al. 1999), assuming that the ICM is isothermal and its density profile follows $\rho_{\rm gas}(r) = \rho_{\rm gas}(0)[1 + (r/r_c)^2]^{-3\beta/2}$ with the gas core radius r_c. At large radii, $r \gg r_c$, where both of our SZE and weak-lensing observations are sensitive, the total mass density follows $\rho_{\rm tot}(r) \propto r^{-2}$. Thus, we set $\beta = 2/3$ to satisfy our assumption of constant $\rho_{\rm gas}(r)/\rho_{\rm tot}(r)$ at large radius. We adopt the values of r_c and T_X listed in Table 1, taken from X-ray observations, and use $T_{\rm gas}(r) = T_X$ as the gas temperature for this model. At $r \gg r_c$, the $\rho_{\rm tot}(r)$ profile can be approximated by that of an SIS (see Section 4.5.1) parameterized by the isothermal one-dimensional velocity dispersion σ_v (see Table 4), constrained by the Subaru distortion data (see Section 4.5).

Requiring hydrostatic balance gives an isothermal temperature $T_{\rm SIS}$, equivalent to σ_v, as

$$k_B T_{\rm SIS} \equiv \mu m_p \sigma_v^2 \frac{2}{3\beta}. \tag{35}$$

For $\beta = 2/3$, $k_B T_{\rm SIS} = \mu m_p \sigma_v^2$, which can be compared with the observed T_X (Table 1). For our AMiBA-lensing cluster sample, we found X-ray to SIS temperature ratios $T_X/T_{\rm SIS} = 0.82 \pm 0.03, 1.65 \pm 0.15, 0.94 \pm 0.05$, and 1.28 ± 0.15 for A1689, A2142, A2261, and A2390, respectively. For A2261 and A2390, the inferred temperature ratios are consistent with unity at 1σ–2σ. For the merging cluster A2142, the observed spatially averaged X-ray temperature (cooling-flow corrected; see Markevitch 1998) is significantly higher than the lensing-derived temperature. This temperature excess of $\sim 4\sigma$ could be explained by the effects of merger boosts, as discussed in Okabe & Umetsu (2008). The temperature ratio $T_X/T_{\rm SIS}$ for A1689, on the other hand, is significantly lower than unity. Recently, a similar level of discrepancy was also found in Lemze et al. (2008a), who performed a careful joint X-ray and lensing analysis of this cluster. A deprojected three-dimensional temperature profile was obtained using a model-independent approach to the *Chandra* X-ray emission measurements and the projected mass profile obtained from the joint strong/weak-lensing analysis of Broadhurst et al. (2005a). The projected temperature profile predicted from their joint analysis exceeds the observed temperature by 30% at all radii, a level of discrepancy suggested from hydrodynamical simulations that find that denser, more X-ray luminous small-scale structure can bias X-ray temperature measurements downward at about the same level (Kawahara et al. 2007). If we accept this +30% correction for T_X, the ratio $T_X/T_{\rm SIS} \to 1.07 \pm 0.04$ for A1689, consistent with $\beta = 2/3$.

6.3. AMiBA SZE Data

We use our AMiBA data to constrain the remaining normalization parameter for the $\rho_{\rm gas}(r)$ profile, $\rho_{\rm gas}(0)$. The calibrated output of the AMiBA interferometer, after the lag-to-visibility transformation (Wu et al. 2009), is the complex visibility $V(\boldsymbol{u})$ as a function of baseline vector in units of wavelength, $\boldsymbol{u} = \boldsymbol{d}/\lambda$, given as the Fourier transform of the sky brightness distribution $\Delta I(\boldsymbol{\theta})$ attenuated by the antenna primary beam pattern $A(\boldsymbol{\theta})$.

In targeted AMiBA observations at 94 GHz, the sky signal $\Delta I(\boldsymbol{\theta})$ with respect to the background (i.e., atmosphere and the mean CMB intensity) is dominated by the thermal SZE due to hot electrons in the cluster, $\Delta I_{\rm SZE} = I_{\rm norm}\, g(\nu) y$ (see Equation (1)). The Comptonization parameter y is expressed as a line-of-sight integral of the thermal electron pressure (see Equation (2)). In the line-of-sight projection of Equation (2), the cutoff radius $r_{\rm max}$ needs to be specified. We take $r_{\rm max} \equiv \alpha_r r_{\rm vir}$ with a dimensionless constant α_r which we set to $\alpha_r = 2$. In the present study, we found that the line-of-sight projection in Equation (2) is insensitive to the choice of α_r as long as $\alpha_r \gtrsim 1$.

A useful measure of the thermal SZE is the integrated Comptonization parameter $Y(\theta)$,

$$Y(\theta) = 2\pi \int_0^\theta d\theta'\, \theta' y(\theta'), \tag{36}$$

which is proportional to the SZE flux, and is a measure of the thermal energy content in the ICM. The value of Y is less sensitive to the details of the model fitted than the central Comptonization parameter $y_0 \equiv y(0)$, with the current configuration of AMiBA. If the $A(\boldsymbol{\theta})y(\boldsymbol{\theta})$ field has reflection symmetry about the pointing center, then the imaginary part of $V(\boldsymbol{u})$ vanishes, and the sky signal is entirely contained in the real visibility flux. If the $A(\boldsymbol{\theta})y(\boldsymbol{\theta})$ field is further azimuthally symmetric, the real visibility flux is expressed by the Hankel

Table 5
AMiBA Visibility Analysis

Cluster	KS01		Isothermal $\beta(=2/3)$	
	y_0 (10^{-4})	$Y(3')$ (10^{-10})	y_0 (10^{-4})	$Y(3')$ (10^{-10})
A1689	4.15 ± 1.00	$2.5^{+0.6}_{-0.6}$	4.31 ± 1.10	$2.6^{+0.6}_{-0.6}$
A2142	2.29 ± 0.28	$3.5^{+0.5}_{-0.5}$	2.00 ± 0.25	$4.0^{+0.5}_{-0.5}$
A2261	3.00 ± 0.84	$1.5^{+0.5}_{-0.4}$	4.25 ± 1.22	$1.6^{+0.5}_{-0.4}$
A2390	2.87 ± 0.61	$1.9^{+0.6}_{-0.5}$	3.40 ± 0.72	$2.1^{+0.8}_{-0.5}$

Notes. The effects of radio point source contamination in the thermal SZE have been corrected (see Liu et al. 2009). The relativistic correction to the SZE is also taken into account.

transform of order zero as

$$V^{Re}(u) = 2\pi I_{\rm norm} g(\nu_c) \int_0^\infty d\theta\, \theta A(\theta) y(\theta) J_0(2\pi u\theta)$$
$$\equiv 2\pi I_0 \int_0^\infty d\theta\, \theta A(\theta) \frac{y(\theta)}{y_0} J_0(2\pi u\theta), \quad (37)$$

where $I_0 = I_{\rm norm} g(\nu_c) y_0$ is the central SZE intensity at $\nu_c = 94$ GHz, $J_0(x)$ is the Bessel function of the first kind and order zero, and $A(\theta)$ is well approximated by a circular Gaussian with FWHM $= 1.22(\lambda/D) \simeq 23'$ at $\nu_c = 94$GHz with an antenna diameter of $D = 60$cm (Wu et al. 2009). The observed imaginary flux can be used to check for the effects of primary CMB and radio source contamination (Liu et al. 2009). From our AMiBA data, we derive in the Fourier domain azimuthally averaged visibility profiles $\langle V(u)\rangle$ for individual clusters.

We constrain the normalization I_0 from χ^2 fitting to the $\langle V(u)\rangle$ profile (Liu et al. 2009). In order to convert I_0 into the central Comptonization parameter, we take account of (1) the relativistic correction $\delta_{\rm SZE}(\nu, T_{\rm gas})$ in the SZE spectral function $g(\nu)$ (see Equation (3)) and (2) corrections for contamination by discrete radio point sources (Liu et al. 2009). The level of contamination in I_0 from known discrete point sources has been estimated to be about 6%–35% in our four clusters (Liu et al. 2009). In all cases, a net positive contribution of point sources was found in our two-patch differencing AMiBA observations (Section 3), indicating that there are more radio sources toward clusters than in the background (Liu et al. 2009). Thus ignoring the point source correction would systematically bias the SZE flux estimates, leading to an underestimate of y_0. The relativistic correction to the thermal SZE is 6%–7% in our T_X range at 94 GHz.

Table 5 summarizes, for our two models, the best-fitting parameter, y_0, and the Y-parameter interior to a cylinder of radius $\theta = 3'$ that roughly matches the AMiBA synthesized beam with $6'$ FWHM. For each case, both cluster models yield consistent values of y_0 and $Y(3')$ within 1σ; in particular, the inferred values of $Y(3')$ for the two models are in excellent agreement. Following the procedure in Section 6.1, we convert y_0 into the central gas mass density, $\rho_{\rm gas}(0)$.

6.4. Gas Mass Fraction Profiles

We derive cumulative gas fraction profiles,

$$f_{\rm gas}(< r) = \frac{M_{\rm gas}(< r)}{M_{\rm tot}(< r)}, \quad (38)$$

for our cluster sample using two sets of cluster models described in Section 6.2, where $M_{\rm gas}(< r)$ and $M_{\rm tot}(< r)$ are the hot gas and total cluster masses contained within a spherical radius r. In Table 6 we list, for each of the clusters, $M_{\rm gas}$ and $f_{\rm gas}$ within r_{2500}, r_{500}, and r_{200} (see also Table 4) calculated with the two models. Note that our total mass estimates do not require the assumption of hydrostatic balance, but are determined based solely on the weak-lensing measurements. Gaussian error propagation was used to derive the errors on $M_{\rm gas}(< r)$ and $f_{\rm gas}(< r)$. We propagate errors on the individual cluster parameters (Tables 1 and 4) by a Monte Carlo method. For A2142, the isothermal model increasingly overpredicts $f_{\rm gas}$ at all radii $r > r_{2500}$, exceeding the cosmic baryon fraction $f_b = \Omega_b/\Omega_m = 0.171 \pm 0.009$ (Dunkley et al. 2009). For other clusters in our sample, both cluster models yield consistent $f_{\rm gas}$ and $M_{\rm gas}$ measurements within the statistical uncertainties from the SZE and weak-lensing data.

Our SZE/weak-lensing-based measurements can be compared with other X-ray and SZE measurements. Grego et al. (2001b) derived gas fractions for a sample of 18 clusters from 30 GHz SZE observations with BIMA and OVRO in combination with published X-ray temperatures. They found $f_{\rm gas}(< r_{500}) = 0.140^{+0.041}_{-0.047} h_{70}^{-1}$ and $0.053^{+0.139}_{-0.031} h_{70}^{-1}$ ($h_{70} = h/0.7$) for A1689 and A2261, respectively, in agreement with our results. For A2142, the $f_{\rm gas}$ and $M_{\rm gas}$ values inferred from the KS01 model are in good agreement with those from the VSA SZE observations at 30 GHz (Lancaster et al. 2005), $M_{\rm gas}(r_{500}) = 6.1^{+1.7}_{-1.8} \times 10^{13}\, M_\odot\, h^{-2}$ and $f_{\rm gas}(r_{500}) = 0.123^{+0.080}_{-0.050} h_{70}^{-1}$. From a detailed analysis of *Chandra* X-ray data, Vikhlinin et al. (2006) obtained $f_{\rm gas}(< r_{500}) = (0.141 \pm 0.009) h_{72}^{-3/2}$ ($h_{72} = h/0.72$) for A2390, in good agreement with our results.

Furthermore, it is interesting to compare our results with the detailed joint X-ray and lensing analysis of A1689 by Lemze et al. (2008a), who derived deprojected profiles of $\rho_{\rm tot}(r)$, $\rho_{\rm gas}(r)$, and $T_{\rm gas}(r)$ assuming hydrostatic equilibrium, using a model-independent approach to the *Chandra* X-ray emission profile and the projected lensing mass profile of Broadhurst et al. (2005a). A steep three-dimensional mass profile was obtained by this approach, with the inferred concentration of $c_{\rm vir} = 12.2^{+0.9}_{-1.0}$, consistent with the detailed lensing analysis of Broadhurst et al. (2005a) and Umetsu & Broadhurst (2008), whereas the observed X-ray temperature profile falls short of the derived profile at all radii by a constant factor of $\sim 30\%$ (see Section 6.2.2). With the pressure profile of Lemze et al. (2008a) we find $y_0 = (4.7 \pm 0.3) \times 10^{-4}$, which is in agreement with our KS01 prediction, $y_0 = (4.2 \pm 1.0) \times 10^{-4}$ (Table 5). The integrated Comptonization parameter predicted by the Lemze et al. model is $Y(3') = (3.0 \pm 0.1) \times 10^{-10}$, which roughly agrees with the AMiBA measurement of $Y(3') = (2.5 \pm 0.6) \times 10^{-10}$. Alternatively, adopting the observed temperature profile in the Lemze et al. (2008a) model reduces the predicted SZE signal by a factor of $\sim 30\%$, yielding $y_0 \simeq 3.3 \times 10^{-4}$ and $Y(3') \simeq 2.1 \times 10^{-10}$, again in agreement with the AMiBA measurements. Therefore, more accurate SZE measurements are required to further test and verify this detailed cluster model.

We now use our data to find the average gas fraction profile over our sample of four hot X-ray clusters. The weighted average of $M_{\rm vir}$ in our AMiBA-lensing sample is $\langle M_{\rm vir}\rangle = (1.19 \pm 0.08) \times 10^{15}\, M_\odot\, h^{-1}$, with a weighted-mean concentration of $\langle c_{\rm vir}\rangle = 8.9 \pm 0.6$. The weighted average of the cluster virial radius is $\langle r_{\rm vir}\rangle \simeq 1.95\, {\rm Mpc}\, h^{-1}$. At each radius we compute the sample-averaged gas fraction, $\langle f_{\rm gas}(< r)\rangle$, weighted by the inverse square of the statistical 1σ uncertainty. In Figure 9, we show for the two models the resulting $\langle f_{\rm gas}\rangle$ profiles as a function

Table 6
Cluster Gas Properties Derived from the AMiBA/Subaru Data

Cluster	KS01 + NFW						Isothermal $\beta(=2/3)$ + SIS					
	$M_{\rm gas,2500}$	$M_{\rm gas,500}$	$M_{\rm gas,200}$	$f_{\rm gas,2500}$	$f_{\rm gas,500}$	$f_{\rm gas,200}$	$M_{\rm gas,2500}$	$M_{\rm gas,500}$	$M_{\rm gas,200}$	$f_{\rm gas,2500}$	$f_{\rm gas,500}$	$f_{\rm gas,200}$
	($10^{13}\,M_\odot h^{-2}$)						($10^{13}\,M_\odot h^{-2}$)					
A1689	$4.4^{+1.1}_{-2.2}$	$8.8^{+2.3}_{-2.2}$	$11.5^{+3.0}_{-3.0}$	$0.098^{+0.025}_{-0.026}$	$0.115^{+0.029}_{-0.029}$	$0.119^{+0.031}_{-0.030}$	$3.5^{+0.9}_{-0.8}$	$7.8^{+2.0}_{-1.8}$	$11.8^{+3.0}_{-2.7}$	$0.100^{+0.024}_{-0.023}$	$0.108^{+0.026}_{-0.025}$	$0.111^{+0.027}_{-0.026}$
A2142	$2.3^{+0.4}_{-1.3}$	$7.2^{+1.5}_{-1.3}$	$11.2^{+2.6}_{-2.2}$	$0.128^{+0.036}_{-0.025}$	$0.169^{+0.046}_{-0.034}$	$0.183^{+0.049}_{-0.037}$	...	...	...	...	...	...
A2261	$3.0^{+0.9}_{-2.1}$	$6.3^{+1.9}_{-2.1}$	$8.4^{+2.7}_{-2.8}$	$0.087^{+0.030}_{-0.028}$	$0.103^{+0.036}_{-0.033}$	$0.108^{+0.040}_{-0.035}$	$2.5^{+0.7}_{-0.7}$	$5.4^{+1.5}_{-1.5}$	$8.1^{+2.3}_{-2.3}$	$0.097^{+0.030}_{-0.028}$	$0.103^{+0.031}_{-0.030}$	$0.105^{+0.032}_{-0.030}$
A2390	$2.3^{+0.7}_{-1.8}$	$6.1^{+2.4}_{-1.8}$	$8.8^{+4.0}_{-2.7}$	$0.122^{+0.059}_{-0.037}$	$0.153^{+0.075}_{-0.049}$	$0.164^{+0.084}_{-0.053}$	$2.2^{+0.6}_{-0.6}$	$5.6^{+1.5}_{-1.5}$	$8.8^{+2.4}_{-2.4}$	$0.125^{+0.035}_{-0.034}$	$0.145^{+0.041}_{-0.041}$	$0.151^{+0.042}_{-0.043}$

Notes. The derived gas fractions $f_{\rm gas}$ scale with the Hubble parameter h as $f_{\rm gas} \propto h^{-1}$ ($h = 0.7$ adopted here). Confidence intervals are quoted at the 1σ (68%) level. Here, we exclude the results from the isothermal model for A2142 which overpredicts $f_{\rm gas}$ at all relevant radii ($r > r_{2500}$) compared with the cosmic baryon fraction, $f_b = \Omega_b/\Omega_m = 0.171 \pm 0.009$.

of radius in units of $r_{\rm vir}$, along with the published results for other X-ray and SZE observations. Here, the uncertainties (cross-hatched) represent the standard error (1σ) of the weighted mean at each radius point, including both the statistical measurement uncertainties and cluster-to-cluster variance. Note that A2142 has been excluded for the isothermal case (see above). The averaged $\langle f_{\rm gas}\rangle$ profiles derived for the isothermal and KS01 models are consistent within 1σ at all radii, and lie below the cosmic baryon fraction $f_b = 0.171 \pm 0.009$ constrained by the *WMAP* five-year data (Dunkley et al. 2009). At $r = \langle r_{200}\rangle \simeq 0.79\langle r_{\rm vir}\rangle$, the KS01 model gives

$$\langle f_{\rm gas,200}\rangle = 0.133 \pm 0.020 \pm 0.018, \quad (39)$$

where the first error is statistical, and the second is the standard error due to cluster-to-cluster variance. This is marginally consistent with $\langle f_{\rm gas,200}\rangle = 0.109 \pm 0.013$ obtained from the averaged SZE profile of a sample of 193 X-ray clusters ($T_X > 3$ keV) using the *WMAP* three-year data (Afshordi et al. 2007). A similar value of $\langle f_{\rm gas,200}\rangle = 0.11 \pm 0.03$ was obtained by Biviano & Salucci (2006) for a sample of 59 nearby clusters from the ESO Nearby Abell Cluster Survey, where the total and ICM mass profile are determined by their dynamical and X-ray analyses, respectively. At $r = \langle r_{500}\rangle \simeq 0.53\langle r_{\rm vir}\rangle$, we have

$$\langle f_{\rm gas,500}\rangle = 0.126 \pm 0.019 \pm 0.016 \quad (40)$$

for the KS01 model, in good agreement with the *Chandra* X-ray measurements for a subset of six $T_X > 5$ keV clusters in Vikhlinin et al. (2006). At $r = \langle r_{2500}\rangle \simeq 0.25\langle r_{\rm vir}\rangle$, which is close to the resolution limit of AMiBA7, we have for the KS01 model

$$\langle f_{\rm gas,2500}\rangle = 0.105 \pm 0.015 \pm 0.012, \quad (41)$$

again marginally consistent with the *Chandra* gas fraction measurements in 26 X-ray luminous clusters with $T_X > 5$ keV (Allen et al. 2004).

7. DISCUSSION AND CONCLUSIONS

We have obtained secure, model-independent profiles of the lens distortion and projected mass (Figures 5 and 6) by using the shape-distortion measurements from high-quality Subaru imaging, for our AMiBA-lensing sample of four high-mass clusters. We utilized weak-lensing dilution in deep Subaru color images to define color–magnitude boundaries for blue/red galaxy samples, where a reliable weak-lensing signal can be derived, free of unlensed cluster members (Figure 3). Cluster contamination otherwise preferentially dilutes the inner lensing signal leading to spuriously shallower profiles. With the observed lensing profiles, we have examined cluster mass–density profiles dominated by DM. For all of the clusters in our sample, the lensing profiles are well described by the NFW profile predicted for collisionless CDM halos.

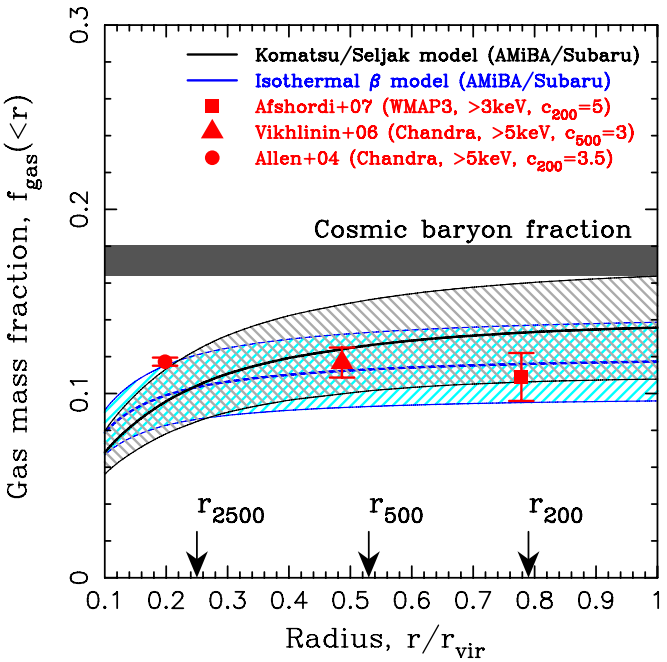

Figure 9. Gas mass fraction profiles $\langle f_{\rm gas}(<r)\rangle = \langle M_{\rm gas}(<r)/M_{\rm tot}(<r)\rangle$ averaged over the sample of four hot ($T_X > 8$ keV) clusters (A1689, A2142, A2261, and A2390) obtained from joint AMiBA SZE and Subaru weak-lensing observations, shown for the NFW-consistent (Komatsu & Seljak 2001) model (black) and the isothermal β model with $\beta = 2/3$ (blue), along with published results (square, triangle, and circle) from other X-ray and SZE observations. The isothermal results exclude the cluster A2142 (see Section 6.4). For each model, the cross-hatched region represents 1σ uncertainties for the weighted mean at each radius point, including both the statistical measurement uncertainties and cluster-to-cluster variance. The black horizontal bar shows the constraints on the cosmic baryon fraction from the *WMAP* five-year data.

A qualitative comparison between our weak-lensing and SZE data, on scales $r \gtrsim 3'$ limited by the current AMiBA resolution, shows a good correlation between the distribution of mass (weak lensing) and hot baryons (SZE) in massive cluster environments (Section 4.4), as physically expected for high-mass clusters with deep gravitational potential wells (Section 4.4). We have also examined and compared, for the first time, the cluster ellipticity and orientation profiles on mass and ICM structure in the Subaru weak-lensing and AMiBA SZE observations, respectively. For all of the four clusters, the mass and ICM distribution shapes are

in good agreement at all relevant radii in terms of both ellipticity and orientation (Figure 8). In the context of the CDM model, the mass density, dominated by collisionless DM, is expected to have a more irregular and elliptical distribution than the ICM density due to inherent triaxiality of CDM halos. We do not see such a tendency in our lensing and SZE data sets, although our ability to find such effects is limited by the resolution of the current AMiBA SZE measurements.

We have obtained cluster gas fraction profiles (Figure 9) for the AMiBA-lensing sample ($T_X > 8$ keV) based on joint AMiBA SZE and Subaru weak-lensing observations (Section 6.4). Our cluster gas fraction measurements are overall in good agreement with previously published values. At $r = \langle r_{200}\rangle \simeq 0.79\langle r_{\rm vir}\rangle$, corresponding roughly to the maximum available radius in our joint SZE/weak-lensing data, the sample-averaged gas fraction is $\langle f_{\rm gas,200}\rangle = 0.133 \pm 0.027$ for the NFW-consistent KS01 model, representing the average over our high-mass cluster sample with a mean virial mass of $\langle M_{\rm vir}\rangle = (1.2\pm0.1)\times10^{15}\,M_\odot\,h^{-1}$. When compared to the cosmic baryon fraction f_b, this indicates $\langle f_{\rm gas,200}\rangle/f_b = 0.78\pm0.16$, i.e., (22 ± 16)% of the baryons is missing from the hot phase in our cluster sample (see Afshordi et al. 2007; Crain et al. 2007). This missing cluster baryon fraction is partially made up by observed stellar and cold gas fractions of $\sim$ several % in our T_X range (Gonzalez et al. 2005).

Halo triaxiality may affect our projected total and gas mass measurements based on the assumption of spherical symmetry, producing an orientation bias. A degree of triaxiality is inevitable for collisionless gravitationally collapsed structures. The likely effect of triaxiality on the measurements of lensing properties has been examined analytically (Oguri et al. 2005; Sereno 2007; Corless & King 2007), and in numerical investigations (Jing & Suto 2002; Hennawi et al. 2007). The effect of triaxiality will be less for the collisional ICM, which follows the gravitational potential and will be more spherical and more smoothly distributed than the total mass–density distribution. For an unbiased measurement of the gas mass fractions, a large, homogeneous sample of clusters would be needed to beat down the orientation bias.

Possible biases in X-ray spectroscopic temperature measurements (Mazzotta et al. 2004; Kawahara et al. 2007) may also affect our gas fraction measurements based on the overall normalization by the observed X-ray temperature. This would need to be taken seriously into account in future investigations with larger samples and higher statistical precision.

Our joint analysis of high-quality Subaru weak-lensing and AMiBA SZE observations allows for a detailed study of individual clusters. The cluster A2142 shows complex mass substructure (Okabe & Umetsu 2008), and displays a shallower density profile with $c_{\rm vir} \sim 5$, consistent with detailed X-ray observations which imply recent interaction. Due to its low z and low $c_{\rm vir}$, the curvature in the lensing profiles is highly pronounced, so that an SIS profile for A2142 is strongly ruled out by the Subaru distortion data alone (Section 4.5.1). For this cluster, our AMiBA SZE map shows an extended structure in the ICM distribution, elongated along the northwest–southeast direction. This direction of elongation in the SZE halo is in good agreement with the cometary X-ray appearance seen by *Chandra* (Markevitch et al. 2000; Okabe & Umetsu 2008). In addition, an extended structure showing some excess SZE can be seen in the northwest region of the cluster. A joint weak-lensing, optical-photometric, and X-ray analysis (Okabe & Umetsu 2008) revealed northwest mass substructure in this SZE excess region, located ahead of the northwest edge of the central gas core seen in X-rays. The northwest mass substructure is also seen in our weak-lensing mass map (Figure 4) based on the much improved color selection for the background sample. A slight excess of cluster sequence galaxies associated with the northwest substructure is also found in Okabe & Umetsu (2008), while no X-ray counterpart is seen in the *Chandra* and *XMM-Newton* images (Okabe & Umetsu 2008). Good consistency found between the SZE and weak-lensing maps is encouraging, and may suggest that the northwest excess SZE is a pressure increase in the ICM associated with the moving northwest substructure. Clearly, further improvements in both sensitivity and resolution are needed if SZE data are to attain a significant detection of the excess structure in the northwest region. Nonetheless, this demonstrates the potential of SZE observations as a powerful tool for measuring the distribution of ICM in cluster outskirts where the X-ray emission measure ($\propto n_e^2$) is rapidly decreasing. This also demonstrates the potential of AMiBA, and the power of multiwavelength cluster analysis for probing the distribution of mass and baryons in clusters. A further detailed multiwavelength analysis of A2142 will be of great importance for further understanding of the cluster merger dynamics and associated physical processes of the intracluster gas.

For A2390, we obtain a highly elliptical mass distribution at all radii from both weak and strong lensing (Frye & Broadhurst 1998). The elliptical mass distribution agrees well with the shape seen by AMiBA in the thermal SZE (Figures 4 and 8). Our joint lensing, SZE, and X-ray modeling leads to a relatively high gas mass fraction for this cluster, $f_{\rm gas,500} \sim 0.15$ for the NFW-consistent case, which is in good agreement with careful X-ray work by Vikhlinin et al. (2006), $f_{\rm gas,500} = (0.141\pm0.009)h_{72}^{-3/2}$.

We have refined for A1689 the statistical constraints on the NFW mass model of Umetsu & Broadhurst (2008), with our improved color selection for the red background sample, where all possible lensing measurements are combined to achieve the maximum possible lensing precision, $M_{\rm vir} = (1.55^{+0.13}_{-0.12})\times10^{15}\,M_\odot\,h^{-1}$ and $c_{\rm vir} = 12.3^{+0.9}_{-0.8}$ (quoted are statistical errors at 68% confidence level), confirming again the high concentration found by detailed lensing work (Broadhurst et al. 2005a; Halkola et al. 2006; Limousin et al. 2007; Umetsu & Broadhurst 2008). The AMiBA SZE measurements at 94 GHz support the compact structure in the ICM distribution for this cluster (Figure 4). Good consistency was found between high-quality multiwavelength data sets available for this cluster (Lemze et al. 2008a, 2008b). Lemze et al. (2008a) performed a joint analysis of *Chandra* X-ray, ACS strong lensing, and Subaru weak-lensing measurements, and derived an improved mass profile in a model-independent way. Their NFW fit to the derived mass profile yields a virial mass of $M_{\rm vir} = (1.58\pm0.15)\times10^{15}\,M_\odot\,h^{-1}$ and a high concentration of $c_{\rm vir} = 12.2^{+0.9}_{-1.0}$, both of which are in excellent agreement with our full lensing constraints. More recently, Lemze et al. (2008b) extended their analysis by including two further high-quality data sets, from VLT/VIRMOS spectroscopy and Subaru/Suprime-Cam imaging. Their dynamical analysis constrains the virial mass of A1689 to be $M_{\rm vir} = (1.3\pm0.4)\times10^{15}M_\odot\,h^{-1}$ and the concentration parameter to be $c_{\rm vir} \geqslant 13.4$ (at 1σ confidence level), in agreement, within about 1σ errors, with our independent lensing analysis and the joint X-ray/lensing analysis of Lemze et al. (2008a). We remark that NFW fits to the Subaru outer profiles alone give consistent but somewhat higher concentrations, $c_{\rm vir} \sim 15$ (Table 3; see also Umetsu & Broadhurst 2008 and Broadhurst et al. 2008). This slight discrep-

ancy can be explained by the mass–density slope at large radii ($\theta \gtrsim 5'$) for A1689 being slightly steeper than the NFW profile where the asymptotic decline tends to $\rho_{\rm NFW}(r) \propto r^{-3}$ (see Broadhurst et al. 2005a; Medezinski et al. 2007; Lemze et al. 2008a; Umetsu & Broadhurst 2008; Lemze et al. 2008b). Recent detailed modeling by Saxton & Wu (2008) suggests such a steeper outer density profile in stationary, self-gravitating halos composed of adiabatic DM and radiative gas components. For accurate measurements of the outermost lensing profile, a wider optical/near-infrared wavelength coverage is required to improve the contamination-free selection of background galaxies, including blue background galaxies, behind this rich cluster.

Our Subaru observations have established that A2261 is very similar to A1689 in terms of both weak- and strong-lensing properties: our preliminary strong lens modeling reveals many tangential arcs and multiply lensed images around A2261, with an effective Einstein radius $\theta_{\rm E} \sim 40''$ at $z \sim 1.5$ (Figure 7), which, when combined with our weak-lensing measurements, implies a mass profile well fitted by an NFW model with a concentration $c_{\rm vir} \sim 10$, similar to A1689 (Umetsu & Broadhurst 2008), and considerably higher than theoretically expected for the standard ΛCDM model, where $c_{\rm vir} \sim 5$ is predicted for the most massive relaxed clusters with $M_{\rm vir} \gtrsim 10^{15}\,M_\odot$ (Bullock et al. 2001; Neto et al. 2007; Duffy et al. 2008).

Such a high concentration is also seen in several other well studied massive clusters from careful lensing work (Gavazzi et al. 2003; Kneib et al. 2003; Broadhurst et al. 2005a, 2008; Limousin et al. 2007; Lemze et al. 2008a). The orientation bias due to halo triaxiality can potentially affect the projected lensing measurements, and hence the lensing-based concentration measurement (e.g., Oguri et al. 2005). A statistical bias in favor of prolate structure pointed to the observer is unavoidable at some level, as this orientation boosts the projected surface mass density and hence the lensing signal. In the context of the ΛCDM model, this leads to an increase of ∼18% in the mean value of the lensing-based concentrations (Hennawi et al. 2007). A larger bias of ∼30 up to 50% is expected for CDM halos selected by the presence of large gravitational arcs (Hennawi et al. 2007; Oguri & Blandford 2009). Our cluster sample is identified by their being X-ray/SZE strong, with the added requirement of the availability of high-quality multiband Subaru/Suprime-Cam imaging (see Section 3.2). Hence, it is unlikely that the four clusters are all particularly triaxial with long axes pointing to the observer. Indeed, in the context of ΛCDM, the highly elliptical mass distribution of A2390 would suggest that its major axis is not far from the sky plane, and that its true concentration is higher than the projected measurement $c_{\rm vir} \simeq 7$.

A chance projection of structure along the line of sight may also influence the lensing-based cluster parameter determination. It can locally boost the surface mass density, and hence can affect in a nonlocal manner (see Equation (29)) the tangential distortion measurement that is sensitive to the total interior mass, if this physically unassociated mass structure is contained within the measurement radius. For the determination of the NFW concentration parameter, it can lead to either an under or overestimate of the concentration depending on the apparent position of the projected structure with respect to the cluster center. When the projected structure is well isolated from the cluster center, one way to overcome this problem is to utilize the convergence profile to examine the cluster mass profile, by locally masking out the contribution of known foreground/background structure (see Section 4.5.2 for the case of A2261).

The ongoing upgrade of AMiBA to 13 elements with 1.2 m antennas will improve its spatial resolution and dynamic range, and the 13 element AMiBA (AMiBA13) will be sensitive to structures on scales down to 2′, matching the angular scales probed by ground-based weak-lensing observations (Umetsu et al. 2004). For our initial target clusters, joint constraints with AMiBA7 and AMiBA13 data will complement the baseline coverage, which will further improve our multiwavelength analysis of the relation between mass and hot baryons in the clusters. A joint analysis of complementary high-resolution lensing, SZE, and X-ray observations will be of great interest to address the issue of halo triaxiality and further improve the constraints on cluster density profiles (Sereno 2007). The AMiBA upgrade will also make the instrument faster by a factor of ∼ 60 in pointed observations. Our constraints can be further improved in the near future by observing a larger sample with AMiBA13. A detailed comparison between X-ray-based and SZE/weak-lensing-based gas fraction measurements will enable us to test the degree of clumpiness ($\langle n_e^2\rangle/\langle n_e\rangle^2$) and of hydrostatic balance in hot cluster gas. The high angular resolution (2′) of AMiBA13 combined with dynamically improved imaging capabilities will allow for direct tests of the gas pressure profile in deep single pointed observations (S. M. Molnar et al. 2009, in preparation).

We thank the anonymous referee for providing useful comments. We are grateful to N. Okabe, M. Takada, and Y. Rephaeli for valuable discussions. We thank the Ministry of Education, the National Science Council, and the Academia Sinica for their support of this project. We thank the Smithsonian Astrophysical Observatory for hosting the AMiBA project staff at the SMA Hilo Base Facility. We thank the NOAA for locating the AMiBA project on their site on Mauna Loa. We thank the Hawaiian people for allowing astronomers to work on their mountains in order to study the universe. We thank all the members of the AMiBA team for their hard work. The work is partially supported by the National Science Council of Taiwan under the grant NSC95-2112-M-001-074-MY2. Support from the STFC for M.B. is also acknowledged.

APPENDIX

ONE-DIMENSIONAL MASS RECONSTRUCTION FROM DISTORTION DATA

Following the method developed by Umetsu & Broadhurst (2008), we derive an expression for the discrete convergence profile using a nonlinear extension of weak-lensing aperture densitometry.

A.1. Nonlinear Aperture Mass Densitometry

For a shear-based estimation of the cluster mass profile, we use a variant of weak-lensing aperture densitometry, or the so-called ζ-statistic (Fahlman et al. 1994; Clowe et al. 2000) of the form

$$\begin{aligned}\zeta_{\rm c}(\theta) &\equiv 2\int_{\theta}^{\theta_{\rm inn}} d\ln\theta'\gamma_+(\theta') \\ &\quad + \frac{2}{1-(\theta_{\rm inn}/\theta_{\rm out})^2}\int_{\theta_{\rm inn}}^{\theta_{\rm out}} d\ln\theta'\gamma_+(\theta') \\ &= \bar{\kappa}(\theta) - \bar{\kappa}(\theta_{\rm inn} < \vartheta < \theta_{\rm out}),\end{aligned} \tag{A1}$$

where $\kappa(\theta)$ is the azimuthal average of the convergence field $\kappa(\boldsymbol{\theta})$ at radius θ, $\bar{\kappa}(\theta)$ is the average convergence interior to radius θ, $\theta_{\rm inn}$ and $\theta_{\rm out}$ are the inner and outer radii of the annular background region in which the mean background contribution, $\bar{\kappa}_b \equiv \bar{\kappa}(\theta_{\rm inn} < \vartheta < \theta_{\rm out})$, is defined; $\gamma_+(\theta) = \bar{\kappa}(\theta) - \kappa(\theta)$ is an azimuthal average of the tangential component of the gravitational shear at radius θ (Fahlman et al. 1994), which is observable in the weak-lensing limit: $\gamma_+(\theta) \approx \langle g_+(\theta)\rangle$. This cumulative mass estimator subtracts from the mean convergence $\bar{\kappa}(\theta)$ a constant $\bar{\kappa}_b$ for all apertures θ in the measurements, thus removing any DC component in the control region $\theta = [\theta_{\rm inn}, \theta_{\rm out}]$. Note that the $\bar{\kappa}_b$ is a nonobservable free parameter. This degree of freedom can be used to fix the outer boundary condition, and hence to derive a convergence profile $\kappa(\theta)$.

In the nonlinear regime, $\gamma_+(\theta)$ is not a direct observable. Therefore, nonlinear corrections need to be taken into account in the mass reconstruction process (Umetsu & Broadhurst 2008). In the subcritical regime (i.e., outside the critical curves), $\gamma_+(\theta)$ can be expressed in terms of the averaged tangential reduced shear as $\langle g_+(\theta)\rangle \approx \gamma_+(\theta)/[1-\kappa(\theta)]$ assuming a quasi-circular symmetry in the projected mass distribution (Broadhurst et al. 2005a; Umetsu et al. 2007). This nonlinear Equation (A1) for $\zeta_{\rm c}(\theta)$ can be solved by an iterative procedure: since the weak-lensing limit ($\kappa, |\gamma|, |g| \ll 1$) holds in the background region $\theta_{\rm inn} \leqslant \theta \leqslant \theta_{\rm max}$, we have the following iterative equation for $\zeta_{\rm c}(\theta)$:

$$\zeta_{\rm c}^{(k+1)}(\theta) \approx 2\int_\theta^{\theta_{\rm inn}} d\ln\theta' \langle g_+(\theta)\rangle [1-\kappa^{(k)}(\theta)] + \frac{2}{1-(\theta_{\rm inn}/\theta_{\rm out})^2}\int_{\theta_{\rm inn}}^{\theta_{\rm out}} d\ln\theta' \langle g_+(\theta')\rangle, \quad \text{(A2)}$$

where $\zeta_{\rm c}^{(k+1)}$ represents the aperture densitometry in the $(k+1)$th step of the iteration ($k = 0, 1, 2, \ldots, N_{\rm iter}$); the $\kappa^{(k+1)}$ is calculated from $\zeta_{\rm c}^{(k+1)}$ using Equation (A10). This iteration is preformed by starting with $\kappa^{(0)} = 0$ for all radial bins, and repeated until convergence is reached at all radial bins. For a fractional tolerance of 1×10^{-5}, this iteration procedure converges within $N_{\rm iter} \sim 10$ iterations. We compute errors for $\zeta_{\rm c}$ and κ with the linear approximation.

A.2. Discretized Estimator for the Lensing Convergence

In the continuous limit, the averaged convergence $\bar{\kappa}(\theta)$ and the convergence $\kappa(\theta)$ are related by

$$\bar{\kappa}(\theta) = \frac{2}{\theta^2}\int_0^\theta d\ln\theta' \theta'^2 \kappa(\theta'), \quad \text{(A3)}$$

$$\kappa(\theta) = \frac{1}{2\theta^2}\frac{d(\theta^2\bar{\kappa})}{d\ln\theta}. \quad \text{(A4)}$$

For a given set of annular radii θ_m ($m = 1, 2, \ldots, N$), discretized estimators can be written in the following way:

$$\bar{\kappa}_m \equiv \bar{\kappa}(\theta_m) = \frac{2}{\theta_m^2}\sum_{l=1}^{m-1} \Delta\ln\theta_l \bar{\theta}_l^2 \kappa(\bar{\theta}_l), \quad \text{(A5)}$$

$$\kappa_l \equiv \kappa(\bar{\theta}_l) = \alpha_2^l \bar{\kappa}_{l+1} - \alpha_1^l \bar{\kappa}_l \quad (l = 1, 2, \ldots, N-1), \quad \text{(A6)}$$

where

$$\alpha_1^l = \frac{1}{2\Delta\ln\theta_l}\left(\frac{\theta_l}{\bar{\theta}_l}\right)^2, \qquad \alpha_2^l = \frac{1}{2\Delta\ln\theta_l}\left(\frac{\theta_{l+1}}{\bar{\theta}_l}\right)^2, \quad \text{(A7)}$$

with $\Delta\ln\theta_l \equiv (\theta_{l+1}-\theta_l)/\bar{\theta}_l$ and $\bar{\theta}_l$ being the area-weighted center of the lth annulus defined by θ_l and θ_{l+1}; in the continuous limit, we have

$$\bar{\theta}_l \equiv 2\int_{\theta_l}^{\theta_{l+1}} d\theta' \theta'^2/(\theta_{l+1}^2 - \theta_l^2) = \frac{2}{3}\frac{\theta_l^2 + \theta_{l+1}^2 + \theta_l\theta_{l+1}}{\theta_l + \theta_{l+1}}. \quad \text{(A8)}$$

The technique of the aperture densitometry allows us to measure the azimuthally averaged convergence $\bar{\kappa}(\theta)$ up to an additive constant $\bar{\kappa}_b$, corresponding to the mean convergence in the outer background annulus with inner and outer radii of $\theta_{\rm inn}$ and $\theta_{\rm out}$, respectively:

$$\bar{\kappa}(\theta) = \zeta_{\rm c}(\theta) + \bar{\kappa}_b. \quad \text{(A9)}$$

Substituting Equation (A9) into Equation (A6) yields the desired expression as

$$\kappa(\theta_l) = \alpha_2^l \zeta_{\rm c}(\theta_{l+1}) - \alpha_1^l \zeta_{\rm c}(\theta_l) + (\alpha_2^l - \alpha_1^l)\bar{\kappa}_b. \quad \text{(A10)}$$

Finally, the error covariance matrix of κ_l is expressed as

$$C_{kl} \equiv \langle \delta\kappa_k \delta\kappa_l\rangle = \alpha_2^k\alpha_2^l C^\zeta_{k+1,l+1} + \alpha_1^k\alpha_1^l C^\zeta_{k,l} - \alpha_1^k\alpha_2^l C^\zeta_{k,l+1} - \alpha_2^k\alpha_1^l C^\zeta_{k+1,l}, \quad \text{(A11)}$$

where $C^\zeta_{kl} \equiv \langle \delta\zeta_k \delta\zeta_l\rangle$ is the bin-to-bin error covariance matrix of the aperture densitometry measurements which is calculated by propagating the rms errors $\sigma_+(\theta_l)$ for the tangential shear measurement.

REFERENCES

Afshordi, N., Lin, Y.-T., Nagai, D., & Sanderson, A. J. R. 2007, MNRAS, 378, 293
Allen, S. W., Ettori, S., & Fabian, A. C. 2001, MNRAS, 324, 877
Allen, S. W., Rapetti, D. A., Schmidt, R. W., Ebeling, H., Morris, R. G., & Fabian, A. C. 2008, MNRAS, 383, 879
Allen, S. W., Schmidt, R. W., Ebeling, H., Fabian, A. C., & van Speybroeck, L. 2004, MNRAS, 353, 457
Allen, S. W., Schmidt, R. W., & Fabian, A. C. 2002, MNRAS, 334, L11
Atrio-Barandela, F., Kashlinsky, A., Kocevski, D., & Ebeling, H. 2008, ApJ, 675, L57
Bartelmann, M. 1996, A&A, 313, 697
Bartelmann, M., Narayan, R., Seitz, S., & Schneider, P. 1996, ApJ, 464, L115
Bartelmann, M., & Schneider, P. 2001, Phys. Rep., 340, 291
Benson, B. A., Church, S. E., Ade, P. A. R., Bock, J. J., Ganga, K. M., Henson, C. N., & Thompson, K. L. 2004, ApJ, 617, 829
Bertin, E., & Arnouts, S. 1996, A&AS, 117, 393
Bialek, J. J., Evrard, A. E., & Mohr, J. J. 2001, ApJ, 555, 597
Birkinshaw, M. 1999, Phys. Rep., 310, 97
Biviano, A., & Salucci, P. 2006, A&A, 452, 75
Boehringer, H., Tanaka, Y., Mushotzky, R. F., Ikebe, Y., & Hattori, M. 1998, A&A, 334, 789
Broadhurst, T., Takada, M., Umetsu, K., Kong, X., Arimoto, N., Chiba, M., & Futamase, T. 2005a, ApJ, 619, L143
Broadhurst, T., Umetsu, K., Medezinski, E., Oguri, M., & Rephaeli, Y. 2008, ApJ, 685, L9
Broadhurst, T., et al. 2005b, ApJ, 621, 53
Bullock, J. S., Kolatt, T. S., Sigad, Y., Somerville, R. S., Kravtsov, A. V., Klypin, A. A., Primack, J. R., & Dekel, A. 2001, MNRAS, 321, 559
Capak, P., et al. 2004, AJ, 127, 180
Capak, P., et al. 2007, ApJS, 172, 99
Carlstrom, J. E., Holder, G. P., & Reese, E. D. 2002, ARA&A, 40, 643
Challinor, A., & Lasenby, A. 1998, ApJ, 499, 1
Chen, M.-T., et al. 2009, ApJ, 694, 1664
Clowe, D., Bradač, M., Gonzalez, A. H., Markevitch, M., Randall, S. W., Jones, C., & Zaritsky, D. 2006, ApJ, 648, L109

Clowe, D., Luppino, G. A., Kaiser, N., & Gioia, I. M. 2000, ApJ, 539, 540
Corless, V. L., & King, L. J. 2007, MNRAS, 380, 149
Crain, R. A., Eke, V. R., Frenk, C. S., Jenkins, A., McCarthy, I. G., Navarro, J. F., & Pearce, F. R. 2007, MNRAS, 377, 41
Crittenden, R. G., Natarajan, P., Pen, U.-L., & Theuns, T. 2002, ApJ, 568, 20
Duffy, A. R., Schaye, J., Kay, S. T., & Dalla Vecchia, C. 2008, MNRAS, 390, L64
Dunkley, J., et al. 2009, ApJS, 180, 306
Erben, T., Van Waerbeke, L., Bertin, E., Mellier, Y., & Schneider, P. 2001, A&A, 366, 717
Fahlman, G., Kaiser, N., Squires, G., & Woods, D. 1994, ApJ, 437, 56
Frye, B., & Broadhurst, T. 1998, ApJ, 499, L115
Fukugita, M., Hogan, C. J., & Peebles, P. J. E. 1998, ApJ, 503, 518
Gavazzi, R., Fort, B., Mellier, Y., Pelló, R., & Dantel-Fort, M. 2003, A&A, 403, 11
Gonzalez, A. H., Zabludoff, A. I., & Zaritsky, D. 2005, ApJ, 618, 195
Grego, L., Carlstrom, J. E., Reese, E. D., Holder, G. P., Holzapfel, W. L., Joy, M. K., Mohr, J. J., & Patel, S. 2001a, ApJ, 552, 2
Grego, L., Carlstrom, J. E., Reese, E. D., Holder, G. P., Holzapfel, W. L., Joy, M. K., Mohr, J. J., & Patel, S. 2001b, ApJ, 552, 2
Halkola, A., Seitz, S., & Pannella, M. 2006, MNRAS, 372, 1425
Halverson, N. W., et al. 2008, ApJ, submitted (arXiv:0807.4208)
Hamana, T., et al. 2003, ApJ, 597, 98
Hattori, M., Kneib, J., & Makino, N. 1999, Prog. Theor. Phys. Suppl., 133, 1
Hennawi, J. F., Dalal, N., Bode, P., & Ostriker, J. P. 2007, ApJ, 654, 714
Heymans, C., et al. 2006, MNRAS, 368, 1323
Ho, P. T. P., et al. 2009, ApJ, 694, 1610
Hoekstra, H., Franx, M., Kuijken, K., & Squires, G. 1998, ApJ, 504, 636
Huang, C.-W. L., et al. 2009, ApJ, submitted
Itoh, N., Kohyama, Y., & Nozawa, S. 1998, ApJ, 502, 7
Jain, B., Seljak, U., & White, S. 2000, ApJ, 530, 547
Jing, Y. P., & Suto, Y. 2002, ApJ, 574, 538
Kaiser, N. 1995, ApJ, 439, L1
Kaiser, N., & Squires, G. 1993, ApJ, 404, 441
Kaiser, N., Squires, G., & Broadhurst, T. 1995, ApJ, 449, 460
Kawahara, H., Suto, Y., Kitayama, T., Sasaki, S., Shimizu, M., Rasia, E., & Dolag, K. 2007, ApJ, 659, 257
Kneib, J.-P., et al. 2003, ApJ, 598, 804
Kneissl, R., Jones, M. E., Saunders, R., Eke, V. R., Lasenby, A. N., Grainge, K., & Cotter, G. 2001, MNRAS, 328, 783
Koch, P., et al. 2006, in ESA Special Publication 626, The European Conference on Antennas and Propagation: EuCAP 2006, ed. H. Lacoste & L. Ouwehand (Noordwijk: ESA), 668.1
Koch, P., et al. 2009a, ApJS, 694, 1670
Koch, P., et al. 2009b, ApJ, submitted
Komatsu, E., & Seljak, U. 2001, MNRAS, 327, 1353
Komatsu, E., & Seljak, U. 2002, MNRAS, 336, 1256
Komatsu, E., et al. 2009, ApJS, 180, 330
Kravtsov, A. V., Nagai, D., & Vikhlinin, A. A. 2005, ApJ, 625, 588
Lancaster, K., et al. 2005, MNRAS, 359, 16
Lemze, D., Barkana, R., Broadhurst, T. J., & Rephaeli, Y. 2008a, MNRAS, 386, 1092
Lemze, D., Broadhurst, T., Rephaeli, Y., Barkana, R., Czoske, O., & Umetsu, K. 2008b, ApJ, submitted (arXiv:0810.3129)
Lewis, G. F., Babul, A., Katz, N., Quinn, T., Hernquist, L., & Weinberg, D. H. 2000, ApJ, 536, 623
Limousin, M., et al. 2007, ApJ, 668, 643
Lin, K.-Y., et al. 2009, ApJ, 694, 1629
Liu, G.-C., et al. 2009, ApJ, submitted
Mandelbaum, R., Seljak, U., & Hirata, C. M. 2008, J. Cosmol. Astropart. Phys., JCAP08(2008)06
Markevitch, M. 1998, ApJ, 504, 27
Markevitch, M., Forman, W. R., Sarazin, C. L., & Vikhlinin, A. 1998, ApJ, 503, 77
Markevitch, M., et al. 2000, ApJ, 541, 542
Mason, B. S., Myers, S. T., & Readhead, A. C. S. 2001, ApJ, 555, L11
Mason, B. S., et al. 2003, ApJ, 591, 540
Maughan, B. J., Jones, C., Forman, W., & Van Speybroeck, L. 2008, ApJS, 174, 117
Mazzotta, P., Rasia, E., Moscardini, L., & Tormen, G. 2004, MNRAS, 354, 10
Medezinski, E., et al. 2007, ApJ, 663, 717
Miyazaki, S., et al. 2002, PASJ, 54, 833
Mroczkowski, T., et al. 2009, ApJ, in press (arXiv:0809.5077)
Myers, S. T., Baker, J. E., Readhead, A. C. S., Leitch, E. M., & Herbig, T. 1997, ApJ, 485, 1
Navarro, J. F., Frenk, C. S., & White, S. D. M. 1996, ApJ, 462, 563
Navarro, J. F., Frenk, C. S., & White, S. D. M. 1997, ApJ, 490, 493
Neto, A. F., et al. 2007, MNRAS, 381, 1450
Nishioka, H., et al. 2009, ApJ, 694, 1637
Oguri, M., & Blandford, R. D. 2009, MNRAS, 392, 930
Oguri, M., Takada, M., Umetsu, K., & Broadhurst, T. 2005, ApJ, 632, 841
Okabe, N., & Umetsu, K. 2008, PASJ, 60, 345
Padin, S., et al. 2001, ApJ, 549, L1
Padin, S., et al. 2002, PASP, 114, 83
Pearson, T. J., et al. 2003, ApJ, 591, 556
Press, W. H., Teukolsky, S. A., Vetterling, W. T., & Flannery, B. P. 1992, Numerical Recipes in FORTRAN: The Art of Scientific Computing (3rd ed., Cambridge: Cambridge Univ. Press)
Reese, E. D., Carlstrom, J. E., Joy, M., Mohr, J. J., Grego, L., & Holzapfel, W. L. 2002, ApJ, 581, 53
Rephaeli, Y. 1995, ARA&A, 33, 541
Rines, K., & Geller, M. J. 2008, AJ, 135, 1837
Sanderson, A. J. R., Ponman, T. J., Finoguenov, A., Lloyd-Davies, E. J., & Markevitch, M. 2003, MNRAS, 340, 989
Sasaki, S. 1996, PASJ, 48, L119
Saxton, C. J., & Wu, K. 2008, MNRAS, 391, 1403
Schneider, P., & Seitz, C. 1995, A&A, 294, 411
Sereno, M. 2007, MNRAS, 380, 1207
Spergel, D. N., et al. 2007, ApJS, 170, 377
Sunyaev, R. A., & Zel'dovich, Y. B. 1972, Comm. Ap. Sp. Phys., 4, 173
Umetsu, K., & Broadhurst, T. 2008, ApJ, 684, 177
Umetsu, K., Chiueh, T., Lin, K.-Y., Wu, J.-M., & Tseng, Y.-H. 2004, Mod. Phys. Lett. A, 19, 1027
Umetsu, K., Tada, M., & Futamase, T. 1999, Prog. Theor. Phys. Suppl., 133, 53
Umetsu, K., Takada, M., & Broadhurst, T. 2007, Mod. Phys. Lett. A, 22, 2099
Umetsu, K., Wu, J.-M., Chiueh, T., & Birkinshaw, M. 2005, arXiv:astro-ph/0506065
Vikhlinin, A., Kravtsov, A., Forman, W., Jones, C., Markevitch, M., Murray, S. S., & Van Speybroeck, L. 2006, ApJ, 640, 691
Watson, R. A., et al. 2003, MNRAS, 341, 1057
Worrall, D. M., & Birkinshaw, M. 2006, in Lecture Notes in Physics 693, Physics of Active Galactic Nuclei at all Scales, ed. D. Alloin (Berlin: Springer), 39
Wright, C. O., & Brainerd, T. G. 2000, ApJ, 534, 34
Wu, J.-H. P., et al. 2008, Mod. Phys. Lett. A, 23, 1675
Wu, J.-H. P., et al. 2009, ApJ, 694, 1619
Yagi, M., Kashikawa, N., Sekiguchi, M., Doi, M., Yasuda, N., Shimasaku, K., & Okamura, S. 2002, AJ, 123, 66
Yoshikawa, K., Jing, Y. P., & Suto, Y. 2000, ApJ, 535, 593
Zhang, P., Pen, U.-L., & Wang, B. 2002, ApJ, 577, 555